Authors' Copy

Remote sensing satellite-based structural/alteration mapping for gold exploration in the Ketté goldfield, Eastern Cameroon

Ghislain Ngassam Mbianya[1], Timoleon Ngnotue[1], Jonas Didero Takodjou Wambo[2,*], Sylvestre Ganno[2], Amin Beiranvand Pour[3], Patrick Ayonta Kenne[1], Donald Hermann Fossi[2, 4], Isabelle D. Wolf[5,6]

[1]Department of Earth Sciences, University of Dschang, P.O. Box. 67 Dschang, Cameroon

[2]Department of Earth Sciences, University of Yaoundé I, P.O. Box 812 Yaounde, Cameroon

[3]Institute of Oceanography and Environment (INOS), Universiti Malaysia Terengganu (UMT), 21030 Kuala Nerus, Terengganu, Malaysia

[4]Institute for Geological and Mining Research, P.O. Box 4110, Yaounde, Cameroon

[5]School of Geography and Sustainable Communities, University of Wollongong, Northfields Avenue, Wollongong, NSW 2522, Australia

[6]Centre for Ecosystem Science, University of New South Wales, Sydney, NSW 2052, Australia

*Corresponding author: jonasdidero@gmail.com (J.D. Takodjou Wambo).

Abstract :

In-situ mineral prospecting studies in the tropics face challenging environmental conditions leading to paucity of data and structural mapping of new mineralizations. Here we present the case of the tropical mining goldfield of Ketté in Cameroon to demonstrate remote sensing techniques for mineral exploration purposes. In this investigation Visible Near Infra-Red (VNIR) and Short Wave Infra-Red (SWIR) bands of Landsat-8 (OLI) and Landsat-7 (ETM+) images were used with field data for lineaments and hydrothermal alterations mapping. Semi-automatic and automatic extraction methods were applied through sobel directional filters to detect the contours in the image. PCA, MNF transformation and a band ratio of 4/2, 6/5 and 6/7 were applied to map alteration minerals. The result revealed NE-SW to ENE-WSW main trends. Gold mineralization occurrences are spatially associated with WNW-ESE to NW-SE (110°-140°) ranging lineaments/faults and show a strong correlation with medium to high lineament density zones. Hydrothermal alteration minerals are spatially associated closely with gold occurrences and known mining sites that are structurally controlled by the NE-SW to ENE-WSW shear zone. The high-prospect zones for gold exploration are located along the Mama and Molé fault, Ngoubésseli, Boubara-Koumbé Tiko, Gwé, and Ndambi I-Tezoukpé.

Key words: Remote sensing; Lineament; Alteration mapping; gold exploration; sub-tropical region; Eastern Cameroon.

1. Introduction

In the tropics, prospecting for new mineral deposits is a cumbersome and expensive undertaking due to the challenging environmental conditions. Here we present a case of the challenges involved and techniques to overcome these to locate gold mineralizations in the tropical Ketté

area. The Ketté is located in a subtropical zone within the Eastern Cameroon gold district (Fuh, 1990; Suh et al., 2006; Takodjou Wambo et al., 2016, 2018, 2020; Tata et al., 2018; Vishiti et al., 2019; Ngatcha et al., 2019) in the Pan-African North Equatorial fold belt (PANEFB; Nzenti et al., 1994). The area hosts both primary and alluvial gold mineralizations (Ngassam Mbianya, 2018). Primary mineralization is found in gold-sulphide bearing quartz veins and weathered rocks (Suh et al., 2006; Tata et al., 2018; Ngatcha et al., 2019; Vishiti et al., 2019; Takodjou Wambo et al., 2020), covered under a thick lateritic layer and controlled by shear zones. In-situ mineral prospecting studies are impeded by the scarcity of data on gold mineralizations and the difficulty to create structural lithological maps because of the heavy vegetation, thick lateritic profile and the sporadic distribution of the outcrops.

To overcome the challenges involved in locating gold mineralizations in hostile terrain remote sensing techniques were recommended (Sonbul et al., 2016; Sheikhrahimi et al., 2019; Adiri et al., 2020; Pour et al., 2021a, b). These techniques have become widespread in geology over the past decades due to the increasing number of observation satellites, satellite imagery and improvements of their spatial and spectral resolutions. Lineament and hydrothermal alteration mapping are among the most important applications of remote sensing in the fields of structural geology for the investigation of mesoscale phenomena (Pluijm and Marshak, 1997) and mineral exploration. The study of Lineaments through optical remote sensing constitutes an important decision-making tool for structural geology studies, and provides the foundation for prospecting, exploration and mining (Javhar et al., 2019).

Several authors have demonstrated the effectiveness of remote sensing in tropical regions for structural geology studies and mineral exploration (Hung et al., 2005; Ramli et al., 2009; Hashim et al., 2013; Metang et al., 2014; Pour and Hashim, 2014a, 2015a,b; Takodjou Wambo et al., 2016). The most commonly used lineament extraction techniques include manual and

automatic methods (Ibrahim and Mutua, 2014; Hashim et al., 2013; Gannouni and Gabtni, 2015; Sedrette and Rebaï, 2016; Han et al., 2018; Javhar et al., 2019; Skakni et al., 2020; Beygi et al., 2020; Moradpour et al., 2020). The use of multispectral and hyperspectral remote sensing images has also shown great success in lithological mapping as well as hydrothermal alteration mapping in the tropical to subtropical domain (Pour and Hashim, 2014b; Kumar et al., 2020; Traore et al, 2020; Takodjou Wambo et al., 2020; Andongma et al., 2020), the arid to semiarid domain (Gad and Kusky., 2006; Pena and Abdelsalam., 2006; Zhang et al., 2007; Amer et al., 2010; Zoheir and Emam, 2013; Kumar et al., 2015; Hammam et al., 2018; Ge et al., 2018; Noori et al., 2019; Bolouki et al., 2020), as well as in the Arctic and Antarctic domains (Haselwimmer et al., 2010; Pour et al., 2018a,b, 2019a,b,c,d, 2021a,b).

The most commonly used processing methods involve spectral enhancement methods such as the Band Ratio (BR), Band Combination (BCs), Principal Component Analysis (PCA), Independent Component Analysis (ICA), Minimum Noise Fraction (MNF), Decorrelation Stretch and supervised automatic classification methods such as the Spectral Angle Mapper (SAM), the Support Vector Machine (SVM), Random Forest (RF), Matched filter, Maximum Likelihood classifier, Linear Discriminant Analysis (LDA), Artificial Neural Networks (ANN), and K-Nearest Neighbors (K-NN) (Sultan et al., 1986; Gad and Kusky, 2006; Haselwimmer et al., 2010; Yu et al., 2012; Abedi et al, 2012; Ge et al, 2018; Hammam et al., 2018; Kuhn et al, 2019; Kumar et al, 2020; Rezaei et al, 2020; Shirmard et al., 2020; Sekandari et al., 2020 a,b; Pour et al., 2021a,b).

The formation of hydrothermal deposits involves four key elements: a metal source, a fluid source, a circulation engine and a precipitation site and mechanism (Arndt and Ganino, 2010). Brittle and ductile deformation structures usually contained in shear zones are good sites for precipitation and concentration. Hydrothermal deposits generally show a spatial association

with faults, fractures and ductile-fragile shear zones at different scales (Austin and Blenkisop, 2009; Zoheir and Emam, 2013; Meshkani et al., 2013; Zoheir et al., 2019 a,b). These structures increase the porosity and permeability of rocks, which then act as channels for hydrothermal fluid circulation. Lineaments are the expression of brittle and ductile geological deformation structures of deep origin (Fossen, 2010) and the distribution of hydrothermal gold mineralization is generally controlled by deformation zones. Several authors have demonstrated a close relationship between gold occurrences and the distribution of lineaments (Bonham-Carter, 1985; Al-Mokredi et al., 2007; Meshkani et al., 2013; Yousefi et al., 2018; Pour and Hashim, 2016).

The aims of this study is: (i) to provide some insight on the deformation history and the structures controlling the distribution of gold mineralization in the Ketté gold field, (ii) to map the different hydrothermal alterations of the Precambrian Ketté basement and (iii) to determine the most suitable zones for primary gold mineralization through remote sensing and GIS methods using Landsat-7 ETM+ and Landsat-8 OLI satellite data and field survey data.

2. Geological setting

The Pan-African-North Equatorial Fold Belt (PANEFB) is the main Precambrian unit in Cameroon. It comprises three distinct geodynamic domains: the northern, central and southern domains (Nzenti et al., 1994; Nzenti et al., 1988; Ngnotue et al., 2000). The Ketté area belongs to the central domain, which is an intermediate domain located between the northern and southern part of the PANEFB (Fig. 1). This domain is marked by multiple regionally significant strike-slip faults and contains abundant granitoids with hyperpotassic and calc-alkaline affinity. These granitic rocks intrude on high-grade metamorphic rocks (gneiss and amphibolites) with an elongated shape extending along the NE-SW (Tanko et al., 2005; Njanko et al., 2006; Nzenti et al., 2006; Ganwa et al., 2008; Kouankap et al., 2010; Nzina Ncharé et al., 2010, Kwékam et al.,

2010; Fozing et al., 2019). The area shows a polyphase evolution with four deformation phases (Ngassam Mbianya, 2018; Ganno et al., 2010; Kankeu et al., 2009) and an emplacement in a transpressive context (Kankeu et al., 2009; Ganno et al., 2010).

Gold has been extracted in the Eastern Cameroon gold district for more than a century. The area has been subdivided into 3 sub-districts based on the type of gold deposits and mining activities (Fuh, 1990, Suh et al., 2006; Takodjou Wambo et al., 2016, 2018, 2020) as follows: (1) The Batouri district consists of granite, granodiorite and tonalite, formed by I-type magma of tonalitic affinity and containing enclaves of gneiss (Asaah et al., 2014). Primary gold is found in quartz veins (Suh and Lehmann, 2003; Asaah et al., 2014; Vishiti et al., 2019) and in rock walls altered through hydrothermal alteration with grades of about 103.7 ppm (Tata et al., 2018). This district is confined to the NE-SW oriented shear zones (Suh et al., 2006). Hydrothermal alteration associated with the quartz-gold veins is characterised by silicification, hematite formation, alkaline metasomatism with development of sericite and pyritisation (Suh et al., 2006; Takodjou Wambo et al., 2020); (2) The Bétaré-Oya district that belongs to the Lom series which consists of three lithological units: (i) the metavolcanoclastic unit, (ii) the upper Proterozoic metasedimentary unit, (iii) and the granitic unit consisting of leucogranites, diorites and syn-D_2 granites (Soba, 1989) crosscut by the Bétaré-Oya fault in a NE-SW direction (Kankeu et al., 2009). Lode gold mineralization occurs with sulphide-bearing quartz veins, showing a spatial association with a steeply dipping N30°-N40°-trending brittle-to-ductile shear zone intersected by metasedimentary sequences in the vicinity of small granitic intrusions (Kankeu et al., 2009; Vishiti et al., 2017). The hydrothermal alteration of quartz veins is marked by silicification, sulfidation, sericitization, potassium feldspar alteration, hematization and carbonization. Gold grains are associated with Ag and are sometimes found as inclusions in pyrite (Vishiti et al., 2017); (3) The Boden district, where the Ketté goldfield is located, hosts primary and alluvial

gold mineralizations. Primary mineralization is hosted in c-type mylonites, cataclasites, gold quartz-tourmaline bearing veins and granites of age between 547-572 Ma (K-Ar method; Fuh, 1990) set in a schist belt of Proterozoic age located in NE-SW-trending restricted shear zones (Fuh, 1990, Suh et al., 2006). These are I-type syn- to post-tectonic granites (Takodjou Wambo et al, 2016), weakly aluminous to peraluminous, with calc-alkaline to shoshonitic affinity hosting gold mineralization, that were brecciated, sheared and sericiticised (Ngatcha et al., 2019). Gold and sulphide quartz veins are associated with zones of pyritization, muscovite/sericite, iron oxides, and silicification (Takodjou Wambo et al., 2020). The Kettévast granitic domain hosts migmatites gneisses, schists, quartz diorites (Gazel and Gerad, 1954) and amphibolites enclaves. This granito-gneissic basement presents a monocyclic evolution in the amphibolite facies (Ngassam Mbianya, 2018). Primary gold source and target zones with high metalliferous potential remain poorly known.

3. Methodology

3.1. Data acquisition

The different data used in this work are: (1) Landsat-8 OLI level 1T and Landsat-7 ETM+ satellite images; (2) thematic maps including the Batouri 1/200 000 topographic sheets and the Batouri-E. 1/500 000 geological map (Gazel and Gerard, 1954); and (3) field data. The main characteristics of the Landsat images used are summarized in Table 1. These images were acquired from the USGS online site and correspond to the zone 33 of the Universal Transverse Mercator UTM projection in the WGS 84 reference geodetic system. Landsat images were chosen because their spatial and spectral resolution renders them suitable for lineament mapping. In addition, OLI data have been successfully used in subtropical settings for hydrothermal alteration mapping (Takodjou Wambo et al., 2020: Traore et al., 2020; Andongma et al., 2020)

and are the most used sensor in exploration geology (Adiri et al., 2020). The VNIR, and SWIR portions of the different images have been used except band 1 OLI. The flowchart methodology adopted in this work is shown in Figure 2.

3.2. Pre-processing

Optical remote sensing images generally contain radiometric and geometric errors resulting from the combined effects of the atmosphere, instruments used, sunlight, and topography (Dubois, 1999; Richards and Jia, 2006). These errors manifest themselves in remotely-sensed images in various types of noise which must be minimized in order to reduce their impact on the final maps. Landsat images used in this work feature level 1 precision and terrain correction (level 1T). They are orthorectified using Ground Control points (GCP) and elevation data provided by a Digital Elevation Model (DEM) for topographic displacement which makes them geodetically accurate (http://usgs.gov). The pre-processing of the Landsat-8 data consisted of radiometric calibration and atmospheric corrections using the FLAASH (Fast Line of Sight Atmospheric Analysis of Spectral Hypercubes) module of the ENVI 5.1 software (Javhar et al., 2019; Takodjou Wambo et al., 2020). Atmospheric effects and noise suppression in Landsat 7 images has been carried out using Erdas Imagine 2014 software.

3.3. Processing

3.3.1. Principal Component Analysis (PCA) and Minimum Noise Fraction (MNF)

Landsat images consist of multispectral intercorrelated bands that contain redundant information resulting in noise production while processing them. PCA and MNF techniques are efficient statistical techniques for spectral enhancement of the remote sensing data. They reduce the dimensionality of the data (Sheikhrahimi et al., 2019), condense topographic and spectral characteristics and improve specific spectral characteristics (Liu and Masson, 2009). By

removing redundant data and noise segregation , information becomes concentrated and preserved in several spectral bands that are correlated with each other within a small number of uncorrelated bands called principal components (Loughlin, 1991; Liu and Masson, 2009; Han et al., 2018; Adiri et al., 2017). This type of processing is based on linear algebraic raster operations and multivariate statistics and provide one of the most efficient techniques for image enhancement for lineament detection (Li et al., 2010). Each principal component output contains data from the different input bands (Adiri et al., 2020) and the contribution of each band can be determined by examining eigenvectors. The MNF consists of two successive PCA operations (Kumar et al., 2015; Adiri et al., 2020) that highlight the anomalies contained in the spectral bands which are related to hydrothermal alteration (Traore et al., 2020). These methods are widely used for lithological and hydrothermal alteration mapping (Loughlin, 1991; Zhang et al., 2007; Kumar et al., 2015; Pour and Hashim, 2015a,b,c; Adiri et al., 2016; Liu et al., 2017; Hammam et al., 2018; Kumar et al., 2020; Adiri et al., 2020; Pour et al., 2021a).

3.3.2. Edge enhancement and detection (spatial filtering)

Lineaments are expressed in texture discontinuities such as the edges of relatively homogeneous areas which are associated with high frequencies and strong reflectance transitions characterized by local pixel variations. In this study, we focused on enhancement and geometric-edge-detection methods based on convolution filtering, defined as the movement (pixel by pixel or line by line) of a mask or filter through an image (Moore, 1983). Successive elements of an original image are multiplied by values in the convolution window and the results are grouped together to form the resulting image. Formula (1) represents the 2D convolution equation used. The g(x,y) is the resulting image from the input image f(x,y) attained through the function h(x,y); the latter is usually called the point spread function; x and y are the spatial coordinates of the pixel position.

Equation (2) describes the discrete form of the 2D convolution with (-w,+w) and (-t,+t) representing the range over which the function h(x,y) equals non-zero in both dimensions. The h(x, y) is the Fourier transform or the 'image' of the frequency filtering function H(u, v), u and v, the frequencies in the horizontal and vertical position, respectively, attained through the frequency filtering function (Liu and Masson, 2009).

$$g(x,y) = f(x,y) * h(x,y) \quad (1)$$

$$= \int_{-\infty}^{+\infty}\int_{-\infty}^{+\infty} f(u,v)h(x-u,y-v)dudv$$

$$= \sum_{u=x-w}^{x+w}\sum_{v=y-t}^{y+t} f(u,v)h(x-u,y-v) \quad (2)$$

The edges are linked to high frequencies. High-pass convolution filters remove low-frequency information from the image and enhance high-frequency information, while low-pass or smoothing filters remove high frequencies typically associated with lineaments in the images, and retain low frequencies (Richards and Jia, 2006; Liu and Masson, 2009). The non-directional 2-D high-pass filters of the sobel gradient type were used in the dimensions 7 x 7 (Table 2) which are widely implemented in lineament extraction (Suzen and Toprak, 1998; Ibrahim and Mutua., 2014; Mwaniki et al., 2015; Gannouni and Gabtni, 2015, Aretouyap et al., 2020).

Gradient filters operate by calculating the first derivative of an image in a given direction to measure the rate change in the image. Contours are always associated with the local maximum of the gradient (Dubois, 1999). Equation (3) reflects the principle of the gradient calculation (Liu and Masson, 2009). The $\bar{\imath}$ and $\bar{\jmath}$ are unit vectors in the x and y directions. These filters have been applied in the N-S, NE-SW, E-W and NW-SE directions to enhance lineaments in all directions.

$$\Delta f = \frac{\partial f(x,y)}{\partial x}\bar{i} + \frac{\partial f(x,y)}{\partial y}\bar{j} \quad (3)$$

3.3.3. Lineaments extraction

Lineaments were manually vectorized on the gradient and the PCA-transformed output images. In gradient images, lineaments appear as linear elements associated with abrupt changes in neighbouring pixels corresponding to high absolute gradient values. Additional lineaments have been vectorized from the Batouri-E geological map (Gazel and Gerard, 1954).

Automatic lineament extraction was used to extract lineaments undetected by the previous semi-automatic extraction method. It was carried out using the PCI Geomatica 2012 Line module, which operates in three stages: edge-detection, thresholding and curve extraction. The edge enhancement is produced from the canny algorithm which uses a Gaussian type filter. This algorithm is very efficient for edge detection in images with moderate noise level but produces biased results when the noise level in the image is high (Dubois, 1999). In order to reduce noise levels in our images, we therefore used data from the PCA transformation as input. The parameters used by this module are: the radius of the filter (Radius), the threshold for the edge gradient (GTHR), the threshold for the curve length (LTHR), the threshold for the line fitting error (FTHR), the threshold for the angular difference (ATHR) and the threshold for linking the distance (DTHR). These different parameters are well detailed in the PCI GEOMATICA online resources (www.pcigeomaticas.com/). A test was conducted combining different values for the previous parameters to choose the combination whose output best aligns with reality.

3.3.4. Band combination (BC) and Band ratio (BR)

The BC and BR constitute enhancement techniques commonly used on multispectral optical remote sensing images for hydrothermal alteration mapping to enhance the discrimination criteria between different rock units and associated mineralogy (e.g. Rezaei et al., 2020). Spectral band ratios reduce the effects of topography in remotely-sensed images and enhance specific features

related to the reflectance spectrum of the target rocks (Richards and Jia, 2006). Several band ratios (BRs) are available in the literature for distinguishing hydrothermal alterations.

Gold deposits generally exhibit spatial association with various types of secondary mineralogical assemblages derived from weathering of host rocks. Mapping of these alteration minerals is based on a specific diagnostic spectral signature of the secondary mineralogical assemblages (Pour and Hashim, 2011; Adiri et al., 2018; Sekandari et al., 2020 a,b). Iron oxides such as limonite, hematite and jarosite represent a common mineral group associated with hydrothermal alterations (Hunt, 1977, Pour and Hashim, 2014b) and sulphide-rich deposits (Abhary and Hassani, 2016). Their absorption spectrum tends to be 0.4-1.1 µm due to electronic processes and vibrations generally encountered in the VNIR portion of the electromagnetic spectrum of these minerals. Their reflectance and absorption is high, ranging between 0.63-0.69 µm and 0.45-0.52 µm, respectively. As they are corresponding to Landsat-8 bands 4 and 2 they were mapped using a 4/2 band ratio (Hunt, 1977; Pour and Hashim, 2014b; Pour and Hashim, 2015c; Abhary and Hassani, 2016; Amara et al, 2019; Takodjou Wambo et al, 2020; Traore et al, 2020; Sekandari et al., 2020 a,b). Hydroxyl-bearing carbonates and clay minerals have a specific spectral absorption at 2.1–2.4 µm and reflectance at 1.55–1.75 µm (Hunt, 1977). These alteration minerals tend to have a high absorption at 2.11-2.29 µm (band 7 of Landsat-8) and a high reflectance at 1.57-1.65 µm (band 6 of Landsat-8). They were mapped using a 6/7 band ratio (Sabins, 1999; Pour and Hashim, 2014b; Pour and Hashim, 2015c; Abhary and Hassani, 2016; Amara et al., 2019; Takodjou Wambo et al., 2020; Traore et al., 2020). Ferrous minerals (e.g., olivine, pyroxene) have a spectral signature marked by a strong absorption at 0.845-0.885 µm (band 5 of Landsat-8) and a strong reflectance at 1.56-1.66 µm (band 6 of Landsat-8). They were mapped using a 6/5 band ratio (Gupta, 2017; Abhary and Hassani, 2016; Traore et al., 2020). The

NDVI was calculated to identify and mask vegetation according to this formula: NDVI = (NIR - RED) / (NIR + RED) (Camps-Valls et al., 2012).

3.4. Post-processing

The vector images resulting from the combined semi-automatic and automatic extraction methods contained some lineaments related to human processes. These images were superimposed on the Batouri 1/200 000 topographic map using a GIS software in order to remove those processes not related to tectonic processes. A GIS analysis was carried out in order to study the geospatial information related to the obtained lineaments. This analysis included the statistical study of lineament length, orientation and density. It aimed to provide more information on the nature and distribution of the obtained lineaments and was performed using ArcGIS 10.3.1 and the Stereonet 8 software. Field trips were organised to map the different rocks in the study area; further, to investigate the hydrothermal alteration and the tectonic architecture of its basement rocks as well as to list and study the gold mineralization occurrences. The main difficulty during the field work was the scarcity of outcrops and the thick lateritic cover.

4. Results

4.1. Alteration mapping

The PCA transformation was applied to Landsat-8 OLI and Landsat-7 ETM+ data. The results are presented in the form of eigenvector matrices (Tables 3 and 4). PC8-1 (Landsat-8) and PC1-7 (Landsat-7) contain 78.12% and 79.86%, respectively, of all variance of the datasets. According to Loughlin (1991), this is mainly due to the fact that these PCs receive an overall scene brightness (albedo) which is responsible for the correlation between the different bands. Other PCs highlight particular spectral characteristics, and eigenvalues decrease due to differences in spectral regions and in different bands (Loughlin, 1991; Carranza and Hale, 2002). PC8-1

contains only positive weightings of the individual input bands. PC7-2 contains positive and negative weighting in the visible (1, 2, 3 bands) and infrared (4,5,7 bands) ranges, respectively, and highlights the differences between both of them (Adiri et al., 2018; Sheikhrami et al., 2019).

PC8-1, PC8-2, PC8-3 and PC7-1, PC7-2, PC7-3 contain 99.45% and 98.43%, respectively, of all variance input OLI and ETM+ data. PC2 (PC8-2, PC7-2) and PC3 (PC8-3, PC7-3) contain positive and negative contributions from different bands. These three PCs contain the topography-related information and likely highlight structural features contained in these data with relatively low noise levels. Due to the latter, PC7-1 and PC8-1 were chosen for automatic lineament extraction using the parameters shown in with Table 5. Hashim et al (2013) recommend the use of small Radi values (3-8), a GTHR value of 10-30 and an ATHR value of 3-5 for good edge detection and optimal lineament extraction in densely vegetated areas.

The Crosta's technique (Crosta and Rabelo, 1993; Carranza and Hale, 2002), based on the examination of the eigenvector matrix (Tables 3 and 4) was used to select the best principal component bands (PCs) related to various hydrothermal alterations. Accordingly, PC8-2 shows a moderately positive weighting of band 6 (0.416) and a strong negative weighting of band 5 (-0.689). Ferrous minerals are mapped in bright pixels in this PC8-2 because of the positive sign in the reflective band 6. PC8-4 shows a strong weighting of band 7 (0.787) and band 6 (-0.521) with opposite signs. The clay and carbonate minerals appear in bright pixels after an invert operation was applied due to negative sign in the reflective band 6. PC8-5 is weighted on strongly by both band 2 (0.681) and band 4 (-0.706), again with opposite signs. This PC is able to recognize specific information related to the iron oxide/hydroxide minerals groups in dark pixels because of the negative sign in the reflective band 4. By using the invert operation, iron oxide/hydroxide minerals appear as bright pixels.

PC8-2 highlights ferrous minerals (Figure 3A). These minerals are scattered throughout the study area and are highly concentrated within the central domain along a N-S to E-W direction. In Pc8-5 the iron hydroxides/oxides mineralogical groups are highlighted (Figure 3B). The alteration minerals are scattered and occur mainly in the Lingbim II, Ketté, Bedobo, Kana, Gbiti, Boubara, Gwé and Mbengoté villages. They are also present in the NE portion of the study area and are associated with mining sites. PC8-4 shows clay and carbonate mineral assemblages (Figure 3C). These minerals also exhibit a widespread distribution in the study area and are primarily found in the mining sites. An FCC image was produced for better identification of the hydrothermal alteration zones (Figure 3D). A red colour was assigned to clay and carbonate minerals, a green colour to ferrous minerals and a blue colour to iron oxides/hydroxides. The oxides/hydroxide minerals appear in yellow colours, clay and carbonate minerals in reddish colours and ferrous minerals in green to blue colours.

Several band ratios have also been applied to map the spatial distribution of hydrothermal alterations. Clay and carbonate minerals were mapped using a 6/7 band ratio. The hydrothermal alterations show the highest concentrations within the drained valleys, creating drainage patterns (Figure 4A).The 6/5 band ratio was applied to discriminate ferrous minerals as per distributions shown in Figure 4.B. The minerals concentrate most strongly within the central part of the study area and form elongated bodies along the NNE-SSW and E-W direction. Medium concentrations are found throughout the study area except in the South. The 4/2 band ratio was used to map iron oxide/hydroxide distributions (Figure 4.C). Medium concentrations are scattered across the whole study area north of the Mama Fault while the highest concentrations are restricted to a few key locations. Sabin's ratio was built in an RGB mode (Figure 4D) for a better extraction of various hydrothermal weathering areas and to tease out the relationships between them. Clay minerals

and carbonates appear in a blue colour, ferrous minerals in a green colour and iron oxides/hydroxides in a yellow colour.

4.2. Lineament extraction and analysis

Figure 5 shows the set of lineaments obtained from the post-processing. A total of 1,565 lineaments were extracted, 717 and 848 from the OLI and ETM+ data, respectively. This difference in the number of extracted lineaments could be explained by the different illumination conditions during the image acquisition and by the difference in the sensitivity of the OLI and ETM+ sensors. Overall, the semi-automatic extraction methods resulted in a higher number of lineaments (1009 lineaments) than the automatic detection from the Line extraction (556 lineaments) and parameters used. Figure 6 shows the number of lineaments obtained from each directional filter and from the Line extraction module for the dataset. Using the ETM+ image helps to achieve a better semi-automatic lineament extraction while using the OLI image offered a better automatic lineament extraction. In addition, Sobel N-S directional filtering provided the best gradient images for a manual lineament extraction. The statistical analysis of lineaments as a function of length shows that they range from 63 m to 3954 m for the OLI data (Figure 7A); 54 m to 3707 m for the ETM+ data (Figure 7B). The lineaments lengths ranged between 1000 m to 1200 m covering the highest distribution frequency for all data (Figure 7C). The lengths of the lineaments extracted from automatic and manual methods are approximately equal.

The directions of lineaments obtained from various data were plotted in directional rosettes at 10° intervals in order to evaluate their distribution. The most important directions are in decreasing order: NE-SW to ENE-WSW, WNW-ESE, NW-SE, N-S and NNE-SSW (Figure 8A). The NE-SW, E-W and WNW-ESE directions are highlighted by the OLI image (Figure 8B) while the ETM+ image highlights the NNW-SSE, N-S and ENE-WSW directions (Figure 8C).

The MNF transform was applied to a Landsat 8 image. Following the processing, the different MNF images were analysed and the MNF 1, 2, 3 were retained because they can provide interesting results. Figure 9A displays this result in an RGB-false-colour composite: MNF3 was assigned to red, MNF2 was assigned to green and MNF1 was assigned to blue. This figure allows distinguishing the dendritic and parallel hydrographic patterns which are mostly showing a NE-SW direction and are controlled by geological structures. The vegetation was mapped from the Normalized Difference Vegetation Index (NDVI), that is mainly found in depressions and generally clusters in drained valleys (Figure 9B).

The different mineral types mapped are strongly correlated with the different mining sites and known gold occurrences. The iron oxide/hydroxide minerals are strongly correlate with primary gold occurrences and the known primary gold mining sites. This mineral group constitutes a good guide for primary gold exploration sites in the study area. Secondarily, gold occurs usually in areas of a high iron oxide/hydroxide concentration. These sites show a weak correlation with ferrous, clay and carbonate mineral types. Based on these observations Boubara-Koumbé Tiko, Gwé, and Tezoukpé represent unexploited target zones with high potential to find primary gold.

4.3. Field survey

4.3.1. Rock outcrops and associated alterations

Several outcrops were identified during the fieldwork. This includes biotite granite, biotite and amphibole granite, granodiorite, Migmatite, Mylonite, Orthogneiss, Pink granite, porphyritic granite, gneiss and amphibolite outcrops (Figure 10A-F). Biotite granites, granodiorites and biotite amphibole granites outcrop mainly in dome and slab shapes at the Gogoboua, Banlékoro, Bossa, Tikolo, Mbéké mining sites, and at Tikela and Timangolo. Orthogneisses outcrop mainly

in slab and dome shapes. Pink granite outcrops in slabs and balls at Ketté, “gendarmerie Ketté”, and Bago. These rocks are found mainly to the north of the Mama Fault. Mylonites outcrops are situated South of the Mama Fault. Gneisses and amphibolites outcrop mainly as enclaves within the granites and mylonites. An update of the previous geological map of the study area incorporates data from the current study (Figure 11).

Hydrothermal alterations gradually affect wall rocks within the study area, depending on their mineralogical composition and structure. Several hydrothermal alterations were observed. These contain argillic alterations, phyllic alterations, propylitic alterations, potassic alterations, and silicification, sulfuidation and ferrugination. Phyllic and propylitic alterations are most related to granites, gneisses and amphibolites. Potassic alterations are most related to mylonites. These secondary mineralogical assemblages define distal to intermediate alteration zones. Silicification, sulfuidation and ferrugination are most related to quartz mineralized veins, and closely related to gold mineralization, and they define intermediate to proximal alterations zone.

4.3.2. Type of mineralization

The field work revealed both primary and alluvial gold mineralization (Figure 12A) in the Ketté area. Prospecting for primary gold mineralization remains difficult due to the thick lateritic profile, sometimes reaching 15m. This was possible using mining holes opened up by operators and mining companies in the Kana, Mbéké mining sites, Ngboudourou Foro and Mbengote villages. Primary gold is associated with quartz veins and hydrothermal deposits related to porphyry-type rocks, principally located in the Kana and Mbéké mining sites. Surface and sub-surface indicators of primary gold concentrations are: smoky and/or brecciated quartz veins (Figure 12B), sulphide porphyritic rocks (Figure 12C), mylonites and hydrothermal weathering zones (Figure 12D).

5. Discussion

5.1. Structural significance of lineaments and Structural control of gold mineralization

Fieldwork data were collated to demonstrate the structural significance of the various trends of the obtained lineaments. According to Ngassam Mbianya (2018), the Ketté basement rocks were affected by a ductile-to-brittle deformation classified into four main deformation phases.

The first deformation D_1 involves ductile tectonics characterized by a S_1 foliation structure (Figure 13A) and strongly transposed by D_2 and D_3 deformation phases. It is also marked by P_1 folds and B_1 boudins. The D_2 deformation phase shows a ductile-to-brittle behaviour marking the gradual transition to a shear-zone operation. This phase is characterised by a S_2 magmatic foliation and a Sm_2 mylonitic schistosity (Figure 13B) with a sub-parallel altitude along the N42°E-N83°E (NE-SW to ENE-WSW) directions (Figure 13); the C_2 shearings and strike slip faults (Figure 13C) along the N70°E-N114°E directions; the P_2 folds that show NE-SW to ENE-WSW directions (Figure 13D). The S/C_2 strain-slip schistosity and B_2 boudins are also present in this deformation phase. That is a dextral to sinistral polarity deformation phase with a dominant dextral movement revealed by a detailed study of shear-sense indicators (Figure 13B-C-D). It corresponds to the major pan-African deformation phase responsible of the regional framework (Kankeu et al., 2009; Ganno et al., 2010). Plutonic rocks were set up in a syn-to-post kinematic context during this deformation phase (Ngassam Mbianya, 2018; Takodjou wambo et al., 2018). The D_3 deformation is also a ductile-to-brittle phase marked by an ENE-WSW directions (Figure 14), S_3 mylonitic schistosity, Sc_3 strain-slip schistosity, B_3 asymmetrical boudins, C_3 strike slip and P_3 folds (Figure 13E) in a N-S direction. This phase shows a dextral kinematic deformation with overprints of D_1/D_2 deformation phases with the continuous operation of a shear zone. The

D4 deformation phase involves mainly brittle deformations characterized by joints and veins of variable geometry that intersect the $S_1/S_2/S_3$ surfaces. The fractures (veins and diaclases) show the major directions of NW-SE, E-W, N-S (Figure 13F).

Remote sensing and field data allowed a better understanding of the rocks structure within the Ketté mining basement, which corresponds with a NE-SW to ENE-WSW oriented shear zone with NW-SE, E-W to N-S oriented fractures. These structural field data made it possible to delineate a tectonic setting of the main lineament orientations that had previously been highlighted. The NE-SW and ENE-WSW directions correspond with the S_2/S_3 foliation, C_2 shears and strike slips. The NW-SE and WNW-ESE directions are perpendicular to a maximum stress direction and represent tensile fractures (Pluijm and Marshak, 1997). These fractures correspond to a brittle tectonic emergent during various tectonic episodes. The N-S directions correspond to strike slips that have occurred during the D_3 phase. The NNE-SSW direction corresponds with the main direction of the S_1 foliation which has been transposed by the D_2/D_3 deformations. These different directions also correspond to brittle structures emerging during the relaxation of stresses through D_3 phase and hydraulic fracturing.

According to Takodjou Wambo et al. (2016) and Nguemhe Fils et al. (2020) these various lineament families are compatible with the Riedel's system. The ENE-WSW direction corresponds to a dextral shear plain. The NNE-SSW, NW-SE, E-W and NE-SW directions correspond to P', R', R and P satellite fractures or faults, respectively, and are associated with the main network in Riedel system.

To study the small-scale structural control of the gold mineralization distribution, 64.8 km^2 grids were constructed around the seven key mining sites and known gold occurrences in the Boussia, Bedobo, Kana, Beke chantier, Gbti, Nboudourou-Foro and Mbengoté villages. Figure 15A illustrates various orientations of lineaments in these grids and depicts a 40°to 70° direction.

These results highlight the local control of the gold mineralization distribution by a NE-SW to ENE-WSW small-scale shear zone that would have allowed migration and storage of gold-rich hydrothermal fluids. The development of this shear zone is mainly linked to the D_2 and D_3 deformation phases which transpose the D_1 phase structures. Gold mineralization appears in D_4.

5.2. Relationship between lineament networks and gold ore occurrences

Gold ores generally show a spatial association with fractured zones. In order to study the spatial association between lineament networks and primary gold mineralization occurrences, a lineament density map was created. It shows the lineament number per unit area and was based on the lineament synthesis from both the Landsat-8 OLI and Landsat-7 ETM+ data. Duplicate lineaments due to simultaneous use of several data sources were removed manually. Several authors have used lineament density analysis for the study and prediction of natural tectonic phenomena (e.g. Salui, 2018). The lineament density shows that the anomalies occur along NW-SE and N-S directions. Gold ores are spatially associated with WNW-ESE to NW-SE (110°-140°) oriented major faults. Most of the mined concentrations are located on the Beké Fault. In addition, the known gold ores show a strong spatial correlation with high lineament density zones. Most of the mining sites are concentrated on high to medium lineament density zones (Figure 15B). Several authors demonstrated a spatial association of high lineaments density, fault or fracture zones with gold occurrences using Landsat optical remote sensing and GIS techniques (Bonham-Carter, 1985; Neawsuparp and Charusiri, 2004; Al-Mokredi et al., 2007; Phani, 2014; Takodjou Wambo et al., 2016, 2018; Nguemhe Fils et al., 2018). These results illustrate that the concentration of primary gold mineralizations are governed by lineament (fault/fracture) networks as described by Trippa and Vearncombe (2002) and others (Austin and Blenkinsop, 2009; Meshkani et al., 2013). The low lineament density associated with the Gbiti and Konyata

mining sites could be explained as an alluvial-type of gold concentrations. Their distribution not only depends on pre-existing fracture networks but more so on the topography and watercourse patterns. Based on the density parameters and the control of mineralization by a NE-SW to ENE-WSW shear zone, the best zones for prospecting primary gold mineralizations is found along the Mama fault, Boumbé fault, and the Koumbé and Ngoubésseli.

5.3. Hydrothermal alterations, rocks and associated lineaments

Gold mineralization in Earstern Cameroon corresponds with the location of quartz veins hosted in schists and granitic intrusions (Suh and Lehmann, 2003; Asaah et al., 2014; Ngatcha et al., 2019; Takodjou Wambo et al., 2016, 2018, 2020; Vishiti et al., 2019; Nforba et al., 2020). This mineralization has induced numerous rock wall alterations during circulation, precipitation, hypogenous and supergenous enrichment mechanisms (Suh et al., 2006; Vishiti et al., 2017; Tata et al., 2018; Takodjou Wambo et al., 2020). The Ketté area also hosts gold mineralizations related to quartz veins. The key alterations associated with this mineralization are marked by sericitization, chloritization, kaolinitization, epidotization, hematiation, sulfuidation, ferrugination, silicification, and the k-feldspar formation. Mapping these types of alterations using optical and radar images provides an excellent investigation method for gold exploration in sub-tropical areas (e.g. Takodjou Wambo et al., 2020 in Ngoura-Colomines, Cameroon; Traoré et al., 2020 in the south east of Birao, Central African Republic; Andongma et al., 2020 in North-Western Nigeria; Neh-Fru et al., 2020 in Mayo Kila, North West of Cameroon). The extracted alteration zones display a strong spatial association with gold occurrences (Takodjou Wambo et al., 2020; Andongma et al., 2020). The various alteration maps provided in this investigation for the Ketté area also show a strong correlation with gold occurrences and known mining sites, and they allowed the delineation of new target areas around Gwé, Ndambi I - Tezoukpé and Boubara-

Koumbé Tiko (Figure 3D, 4D). The systematic superposition of primary gold occurrences and iron oxides/hydroxide mineral groups attests the proximal nature of this alteration.

High iron oxides/hydroxides concentrations were associated with porphyritic granites and mylonites. These results are consistent with field data that evidence the presence of pyrite, magnetite and hematite generally pervading these rock types. Clay and carbonate minerals also show a strong association with porphyritic granites and mylonites. They are generally superimposed on iron oxide/hydroxide rich areas and occupy the drainage pattern. This is due to clay-rich alluvium deposits present in the drainage pattern. The high concentrations of ferrous minerals also display a strong spatial association with porphyritic granites. These results show petrographic types as potential surface and subsurface indicators for primary gold occurrences in the Ketté area.

The mapped alteration minerals display a significant correlation with areas of medium to high lineament density, especially iron oxides/hydroxides. Their spatial distribution is well correlated with the spatial distribution of the lineaments and follows the orientation of the main lineaments/faults identified in the study area. This result demonstrates the structural control of hydrothermal alterations by lineaments/faults networks and consequently, the structural control of primary gold distributions.

Conclusion

This investigation highlights the utility of using Landsat-8 OLI and Landsat-7 ETM+ images combined with field data for lineaments mapping and hydrothermal alteration mapping for mineral exploration in the Ketté area. Lineament mapping both automatic and semi-automatic extraction methods enabled to identify predominantly NE-SW to ENE-WSW, WNW-ESE, NW-SE, N-S and NNE-SSW structure trends in the study area. These lineaments are associated with

ductile and brittle structures of a deep origin expression. They can be classified as emergent in four deformation phases as field investigations proved, which exhibit a NE-SW to ENE-WSW oriented shear zone in the study area. Primary mineralization is related to gold-bearing quartz veins and porphyry rocks and shows a close spatial association with major faults in WNW-ESE to NW-SE (110°-140°) directions, including high lineament density areas. They are controlled by a NE-SW to ENE-WSW trending shear zone. Primary gold is also associated with several hydrothermal alterations discriminated and mapped through different image processing techniques. Iron oxides/hydroxides, clay and carbonate minerals show a strong spatial association with porphyritic granite and mylonites. Ferrous minerals show strong spatial associations with porphyritic granite. These various wall rocks show a strong correlation with gold occurrences and known mining sites including areas of medium to high lineament density that are distributed according to the main fault networks revealed by the lineament mapping.

The Mama and Molé fault, Ngoubésseli, Boubara-Koumbé Tiko, Gwé, and Tezoukpé are newly discovered prospect sites revealed by a spatial distribution analysis of lineaments and hydrothermal alterations. Lineament density is a key factor for controlling the spatial distribution of hydrothermal alterations and gold mineralizations in the study area. Their distribution is structurally controlled by a NE-SW to ENE-WSW oriented shear zone.

Acknowledgments

The data presented here form a part of the primary author's Ph.D. thesis supervised by T. Ngnotué at the University of Dschang, Cameroon. We gratefully acknowledge several anonymous reviewers for their critical and constructive comments of the manuscript.

References

Abedi, M., Norouzi, G-H., Bahroudi, A., 2012. Support vector machine for multi-classification of mineral prospectivity areas. Computers & Geosciences 46, 272–283. doi:10.1016/j.cageo.2011.12.014

Abhary, A., Hassani, H., 2016. Mapping Hydrothermal Mineral Deposits Using PCA and BR Methods in Baft 1:100000 Geological Sheet, Iran. International Journal of Advanced Engineering, Management and Science 2 (9)

Adiri, Z., El Harti, A., Jellouli, A., Lhissou, R., Maacha, L., Azmi, M., Zouhair, M., Bachaoui, E.M., 2017. Comparison of Landsat-8, ASTER and Sentinel 1 satellite Remote Sensing data in Automatic Lineaments Extraction: a case study of Sidi Flah-Bouskour inlier, Moroccan Anti Atlas. Advances in Space Research 60, 2355-2367, doi: http://dx.doi.org/10.1016/j.asr.2017.09.006

Adiri, Z., El Harti, A., Jellouli, A., Maacha, L., Azmi, M., Zouhair, M., Bachaoui, E. M., 2018. Mineralogical mapping using Landsat-8 OLI, Terra ASTER and Sentinel-2A multispectral data in Sidi Flah-Bouskour inlier, Moroccan Anti-Atlas. Journal of Spatial Science, 65: 1, 147-171, DOI: 10.1080/14498596.2018.1490213

Adiri, Z., El Harti, A., Jellouli, A., Maacha, L., Bachaoui, E., 2016. Lithological mapping using Landsat 8 OLI and Terra ASTER multispectral data in the Bas Drâa inlier, Moroccan Anti Atlas. Journal of Applied Remote Sensing 10 (1), 016005.

Adiri, Z., Lhissou, R., El Harti, A., Jellouli, A., Chakouri, M., 2020. Recent advances in the use of public domain satellite imagery for mineral exploration: A review of Landsat-8 and Sentinel-2 applications, Ore Geology Reviews 117, doi: https://doi.org/10.1016/j.oregeorev.2020.103332

Amara, B.N., Aissa, D.E., Maouche, S., Braham, M., Machane, D., Guessoum, N., 2019. Hydrothermal alteration mapping and structural features in the Guelma basin (Northeastern Algeria): contribution of Landsat-8 data. Arab J. Geosci. 12:94.

Andongma, W.T., Gajere, J.N., Amuda, A.K., Edmond, R.R.D., Faisal, M., Yusuf, Y.D., 2020. Mapping of hydrothermal alterations related to gold mineralization within parts of the Malumfashi Schist Belt, North-Western Nigeria. The Egyptian Journal of Remote Sensing and Space Sciences xxx (xxxx) xxx. https://doi.org/10.1016/j.ejrs.2020.11.001

Al-Mokredi, M. S., Guangdao, H., Al Bassam, B. F, 2007. Using Remote Sensing Data to Delineate the Lineaments for Hydrothermal Mineral Prediction in Heqing Area, Northwest Yunnan Province, China. Journal of China University of Geosciences, vol. 18, No. 2, p.142-147

Amer, R., Kusky, T., Ghulam, A., 2010. Lithological mapping in the Central Eastern Desert of Egypt using ASTER data. Journal of African Earth Sciences 56, 75–82. doi:10.1016/j.jafrearsci.2009.06.004

Arndt, N. T., Ganino, C., 2010. RESSOURCES MINÉRALES Origine, nature et exploitation. Dunod, Paris, 2010

Aretouyap, Z., Billa, L., Jones, M., Richter, G., 2020. Geospatial and statistical interpretation of lineaments: salinity intrusion in the Kribi-Campo coastland of Cameroon. Advances in Space Research 66, 844–853. https://doi.org/10.1016/j.asr.2020.05.002

Asaah, A.V., Zoheir, B., Lehmann, B., Frei, D., Burgess, R., Suh, C.E., 2014. Geochemistry and geochronology of the ~620 Ma gold-associated Batouri granitoids, Cameroon. Int. Geol. Rev. http://dx.doi.org/10.1080/00206814.2014.951003.

Austin, J. R., Blenkinsop, T.G., 2009. Local to regional scale structural controls on mineralisation and the importance of a major lineament in the eastern Mount Isa Inlier, Australia: Review and analysis with autocorrelation and weights of evidence. Ore Geology Reviews 35, 298–316. doi:10.1016/j.oregeorev.2009.03.004

Bonham-Carter, G. F., 1985. Statistical Association of Gold Occurrences with Landsat-Derived Lineaments, Timmins-Kirkland Lake Area, Ontario. Canadian Journal of Remote Sensing: Journal canadien de télédétection, 11:2, 195-210, DOI:10.1080/07038992.1985.10855089

Beygi, S., Talovina, I.V., Tadayon, M., Pour, A.B., 2020. Alteration and structural features mapping in Kacho-Mesqal zone, Central Iran using ASTER remote sensing data for porphyry copper exploration. International Journal of Image and Data Fusion, Article in press, https://doi.org/10.1080/19479832.2020.1838628

Bolouki, S.M., Ramazi, H.R., Maghsoudi, A., Pour, A.B., Sohrabi, G., 2020. A Remote Sensing-Based Application of Bayesian Networks for Epithermal Gold Potential Mapping in Ahar-Arasbaran Area, NW Iran. Remote Sensing 12, 105. https://doi.org/10.3390/rs12010105

Camps-Valls, G., Tuia, D., Gómez-Chova, L., Jiménez, S., Malo, J., 2012. Remote sensing image processing. Synthesis Lectures on Image, Video, and Multimedia Processing 12, 194P. https://doi.org/10.2200/S00392ED1V01Y201107IVM012

Carranza, E.J.M., Hale, M., 2002. Mineral mapping with Lansat Thematic Mapper data for hydrothermal alteration mapping in heavily vegetated terrain. Int. J. Remote Sens. 23 (22), 4827–4852.

Crosta, A. P., Rabelo, A., 1993. Assessing Landsat TM for hydrothermal alteration mapping in central–western Brazil. Proceedings of the Ninth Thematic Conference on Geologic Remote Sensing, Pasadena, California, USA, 8–11 February 1993 (Ann Arbor, MI: Environmental Research Institute of Michigan), pp. 1053–1061.

Dubois, J., 1999. Identification des linéaments dans les images satellitaires par ajustement et suivi de segments. proj. appl. Maitr. Univ. du Québec, 123P.

Fossen, H. (2010). Structural geology. Cambridge: Cambridge University Press.

Fozing, E.M., Kwékam, M., Gountié, D. M., Asaah, A. N., Njanko, T., Tcheumenak Kouémo, J., Efon Awoum, J., Njonfang, E., 2019. Petrography and geochemistry of amphibolites from the Fomopéa Pluton (West Cameroon): origin and geodynamic setting. Journal of African Earth Sciences 154, 181-194. Doi : 10.1016/j.jafrearsci.,2019.03.024.

Fuh, C.G., 1990. The geochemical and structural controls on gold mineralization in the Colomines area: Pan-African belt of eastern Cameroon. Ph.D. thesis, University of London, UK, 268 p.

Gad, S., Kusky, T., 2006. Lithological mapping in the Eastern Desert of Egypt, the Barramiya area, using Landsat thematic mapper (TM). Journal of African Earth Sciences 44, 196–202. doi:10.1016/j.jafrearsci.2005.10.014

Ganno, S., Nzenti, J.P., Ngnotue, T., Kankeu, B., Kouankap Nono, G.D., 2010. Polyphase deformation and evidence for transpressive tectonics in the Kimbi area, Northwestern Cameroon Pan-African fold belt. Journal of Geology and Mining Research 2(1), 001-015.

Gannouni, S., Gabtni, H., 2015. Structural Interpretation of Lineaments by Satellite Image Processing (Landsat TM) in the Region of Zahret Medien (Northern Tunisia). Journal of Geographic Information System, 7, 119-127. http://dx.doi.org/10.4236/jgis.2015.72011

Ganwa, A. A., Frisch, W., Siebel, W., Shang, C.K., Mvondo Ondoa, J., Satir, M., Tchakounté Numbem, J., 2008. Zircon 207Pb/206Pb evaporation ages of Panafrican metasedimentary

rocks in the Kombé-II area (Bafia Group, Cameroon): Constraints on protolith age and provenance. Journal of African Earth Sciences, 51,77-88.

Gazel, J., Gerad, G., 1954. Notice explicative sur la feuille Batouri- Est : Carte géologique de réconnaissance à l'echelle du 1/500 000. Paris (imprimerie nationale), 42p.

Ge, W., Cheng, Q., Tang, Y., Jing, L., Gao, C., 2018. Lithological Classification Using Sentinel-2A Data in the Shibanjing Ophiolite Complex in Inner Mongolia, China. Remote Sens. 10, 638. doi:10.3390/rs10040638

Gupta, R.P., 2017. Remote Sensing Geology, third ed. Springer, Berlin, Germany, pp.180–190 235-240, and 332-336.

Hammam, A., Gaber, A., Abdelwahed, M., Hammed, M., 2018. Geological mapping of the Central Cairo-Suez District of Egypt, using space-borne optical and radar dataset. The Egyptian Journal of Remote Sensing and Space Sciences 23 (3), 275-285. https://doi.org/10.1016/j.ejrs.2018.11.004

Han L., Liu Z., Ning Y., Zhao Z., 2018. Extraction and analysis of geological lineaments combining a DEM and remote sensing images from the northern Baoji loess area. Advances in Space Research 62, 2480–2493. https://doi.org/10.1016/j.asr.2018.07.030

Haselwimmer, E., Riley, T. R., Liu, J. G., 2010. Assessing the potential of multispectral remote sensing for lithological mapping on the Antarctic Peninsula: case study from eastern Adelaide Island, Graham Land. Antarctic Science 22(3), 299–318. doi:10.1017/S0954102010000015

Hashim, M., Ahmad, S., Md Johari, M.A., Pour, A.B., 2013. Automatic lineament extraction in a heavily vegetated region using Landsat Enhanced Thematic Mapper (ETM+) imagery. Advances in Space Research 51, 874–890

Hung, L. Q., Batelaan, O., De Smedt, F., 2005. Lineament extraction and analysis, comparison of LANDSAT ETM and ASTER imagery. Case study: Suoimuoi tropical karst catchment, Vietnam. Remote Sensing for Environmental Monitoring, GIS Applications, and Geology V, Proc. of SPIE Vol. 5983, 59830T, 0277-786X/05/$15 · doi: 10.1117/12.627699

Hunt, G.R., 1977. Spectral signatures of particulate minerals in the visible and near infrared. Geophysics 42, 501–513.

Ibrahim, U., Mutua, F., 2014. Lineament Extraction using Landsat 8 (OLI) in Gedo, Somalia. International Journal of Science and Research (IJSR), vol 3 issue 9

Javhar, A., Chen, X., Bao, A., Jamshed, A., Yunus, M., Jovid, A., Latipa, T., 2019. Comparison of Multi-Resolution Optical Landsat-8, Sentinel-2 and Radar Sentinel-1 Data for Automatic Lineament Extraction: A Case Study of Alichur Area, SE Pamir. Remote Sens. 2019, 11, 77. doi:10.3390/rs11070778

Kankeu B., Greiling R.O., Nzenti J.P., 2009. Pan-African strike-slip tectonics in eastern Cameroon - magnetic fabrics (AMS) and structure in the Lom basin and its gneissic basement. Precambrian Research (2008).

Kouankap Nono, G.D., Nzenti, J.P., Suh, C.E., Ganno, S., 2010. Geochemistry of Ferriferous, High-K Calc-Alkaline Granitoids from Banefo –Mvoutsaha Massif (NE Bafoussam), Central Domain of the Pan-African Fold Belt, Cameroon. The Open Geology Journal 4, 21-34.

Kuhn, S., Cracknell, M.J., Reading, A.M., 2019. Lithological mapping in the Central African Copper Belt using Random Forests and clustering: Strategies for optimised results. Ore Geology Reviews 112 (2019) 103015. https://doi.org/10.1016/j.oregeorev.2019.103015

Kumar, C., Chatterjee, S., Oommena, T., Guha. A., 2020. Automated lithological mapping by integrating spectral enhancement techniques and machine learning algorithms using AVIRIS-NG hyperspectral data in Gold-bearing granite-greenstone rocks in Hutti, India. Int J Appl Earth Obs Geoinformation 86, 102006. https://doi.org/10.1016/j.jag.2019.102006

Kumar, C., Shetty, A., Raval, S., Sharma, R., Champati Ray, P.C., 2015. Lithological Discrimination and Mapping using ASTER SWIR Data in the Udaipur area of Rajasthan, India. Procedia Earth and Planetary Science 11, 180 – 188. doi: 10.1016/j.proeps.2015.06.022

Kwékam, M., Liégeois, J.P., Njonfang, E., Affaton, P., Hartmann, G., Tchoua, F., 2010. Nature origin and significance of the Pan-African high-K calc-alkaline Fomopéa plutonic complex in the Central African fold belt (Cameroon). Journal of African Earth Sciences 57, 79-95.

Li, N., Frei, M., Altermann, W., 2010. Textural and knowledge-based lithological classification of remote sensing data in Southwestern Prieska sub-basin, Transvaal Supergroup, South Africa. Journal of African Earth Sciences 60 (2011) 237–246. doi:10.1016/j.jafrearsci.2011.03.002

Liu, G. J., Philippa Mason, J. P., 2009. Essential Image Processing and GIS for Remote Sensing. 1st edn, John Wiley & Sons, Ltd, Publication 443P.

Liu, L., Zhou, J., Han, L., Xu, X., 2017. Mineral mapping and ore prospecting using Landsat TM and Hyperion data, Wushitala, Xinjiang, northwestern China. Ore Geology Reviews 81 (1) 280–295. http://dx.doi.org/10.1016/j.oregeorev.2016.10.007

Loughlin, W., 1991. Principal component analysis for alteration mapping. Photogrammetric Engineering and Remote Sensing, 57, 1163–1169.

Meshkani, A. S., Mehrabi, B., Yaghubpur, A., Sadeghi, M., 2013. Recognition of the regional lineaments of Iran: Using geospatial data and their implications for exploration of metallic ore deposits. Ore Geology Reviews 55 (2013) 48–63

Metang, V., Nkoumbou, C., Tchakounté, N.J., Njopwouo, D., 2014. Application of remote sensing for the mapping of geological structures in rainforest area: a case study at the Matomb-Makak area, Center-South Cameroon. Journal of Geosciences and Geomatics, 2(5), 196-207

Moore, G.K., Waltz, F.A., 1983. Objective procedure for lineament enhancement and extraction. Photogrammetric Engineering & Remote Sensing, 49 (5): 641–647.

Moradpour, H., Paydar, G.S., Pour, A.B., Kamran, K.V., Feizizadeh, B., Muslim, M. A., Hossain, M.S., 2020. Landsat-7 and ASTER remote sensing satellite imagery for identification of iron skarn mineralization in metamorphic regions. Geocarto International, Article in press, https://doi.org/10.1080/10106049.2020.1810327

Mwaniki M. W., Moeller M. S., Schellmann G., 2015. A comparison of Landsat 8 (OLI) and Landsat 7 (ETM+) in mapping geology and visualising lineaments: A case study of central region Kenya. The International Archives of the Photogrammetry, Remote Sensing and Spatial Information Sciences, Volume XL-7/W3, 2015, 36th International Symposium on Remote Sensing of Environment, 11–15 May 2015, Berlin, Germany

Neawsuparp, K., Charusiri, P., 2004. Lineaments Analysis Determined from Landsat Data Implication for Tectonic Features and Mineral Occurrences in Northern Loei Area, NE Thailand. ScienceAsia 30 (2004): 269-278

Neh-Fru, M.I., Andongma, W.T., Yongue, R.F., Anaba Fotze, Q.M., 2020. Remote Sensing for Geological Investigation of Mayo Kila and Environs, North West Region of Cameroon. American Journal of Earth Sciences 7 (1), 1-12.

Nforba, M.T., Chi, S.J., Emmanuel, T.T., Kouske, A.P., 2020. Structural and Geochemical Characterization of Gold Mineralized Quartz Veins in Belikombone Gold Prospect, Betare-oya Gold District, East Cameroon. Engineering Science 5 (2),17-26. doi: 10.11648/j.es.20200502.12

Ngassam Mbianya, G. (2018). Étude pétrographique et structurale des formations précambriennes de Ketté (Est-Cameroun): implications métallogéniques. Unpublished Master thesis, University of Dschang, 109p.

Ngatcha, R.B., Okunlola, O.A., Suh, C.E., Ateh, K.I., Hofmann, A., 2019. Petrochemical characterization of Neoproterozoic Colomine granitoids, SE Cameroon: Implications for gold mineralization. Lithos 344–345, 175–192.

Ngnotué, T., Nzenti, J. P., Barbey, P., and Tchoua, F. M., 2000. The Ntui-Betamba highgrade gneisses: à Northward extension of the Pan-African Yaounde gneisses in Cameroon. Journal of African Earth Sciences 31, 369-381.

Nguemhe Fils, S.C., Bekele Mongo, C. H., Nkouathio, D. G., Mimba, M. E., Etouna, J., Njandjock Nouck, P., Brunot Nyeck, B., 2018. Radarsat-1 image processing for regional-scale geological mapping with mining vocation under dense vegetation and equatorial climate environment, Southwestern Cameroon. The Egyptian Journal of Remote Sensing and Space Sciences 21, S43–S54. https://doi.org/10.1016/j.ejrs.2018.05.005

Njanko, T., Nedelec, A., Affaton, P., 2006. Synkinematic high - K calc-alkaline plutons associated to the Pan-African Central Cameroon Shear Zone (W-Tibati area): Petrology and geodynamic significance. Journal of African Earth Sciences 44, 494-510.

Noori, L., Pour, A.B., Askari, G., Taghipour, N., Pradhan, B., Lee, C-W., Honarmand, M., 2019. Comparison of Different Algorithms to Map Hydrothermal Alteration Zones Using ASTER Remote Sensing Data for Polymetallic Vein-Type Ore Exploration: Toroud–Chahshirin Magmatic Belt (TCMB), North Iran. Remote Sensing, 11, 495. https://doi.org/10.3390/rs11050495

Nzenti, J.P., Badibanga Kapajika, G., Wörner Toto, R.L., 2006. Synkinematic emplacement of granitoids in a Pan-African shear zone in Central Cameroon. Journal of African Earth Sciences, 45, 74-86.

Nzenti, J.P., Barbey, P., Bertrand, J.M., Macaudière, J., 1994. La chaîne panafricaine au Cameroun: Cherchons suture et modèle, 15ème Réunion des Sciences de la Terre, Nancy, France, Société Géologique de France, p. 99.

Nzenti, J.P., Barbey, P., Macaudiere, J., Soba, D., 1988. Origin and Evolution of the late Precambrian high-grade Yaoundé gneisses (Cameroon). Precambrian Research 38, 91- 109.

Nzina Nchare, A., Nzenti, J.P., Tanko Njiosseu, E. L., Ganno, S., Ngnotué, T., 2010. Synkinematic ferro-potassic magmatism from the Mekwene-Njimafofire Foumban Massif, along the Foumban-Banyo shear zone in central domain of Cameroon PanAfrican fold belt. Journal of Geology and Mining Research 2(6), 142-158.

Pena, S.A., Abdelsalam, M.G., 2006. Orbital remote sensing for geological mapping in southern Tunisia: Implication for oil and gas exploration. Journal of African Earth Sciences 44, 203–219. doi:10.1016/j.jafrearsci.2005.10.011

Phani, P. R., 2014. A GIS based correlation between lineaments and gold occurrences of Ramagiri- Penakacherlaschist belt, eastern Dharwar craton, INDIA. International Journal of Geology, Earth & Environmental Sciences, Vol. 4 (3), pp. 259-267

Pluijm, V. J., Marshak, 1997. Earth Structure: an introduction to structural geology and tectonics. McGraw Hill, 495pp

Pour, A.B., Hashim, M., 2011. Identification of hydrothermal alteration minerals for exploring of porphyry copper deposit using ASTER data, SE Iran. Journal of Asian Earth Sciences 42, 1309–1323. doi:10.1016/j.jseaes.2011.07.017

Pour, A.B., Hashim, M., 2014a. Structural geology mapping using PALSAR data in the Bau gold mining district, Sarawak, Malaysia. Advances in Space Research, 54 (4), 644-654.https://doi.org/10.1016/j.asr.2014.02.012

Pour, A.B., Hashim, M., 2014b. ASTER, ALI and Hyperion sensors data for lithological mapping and ore minerals exploration. SpringerPlus, 3:130.

Pour, A.B., Hashim, M., 2015a. Structural mapping using PALSAR data in the Central Gold Belt, Peninsular Malaysia. Ore Geology Reviews 64, 13-22. https://doi.org/10.1016/j.oregeorev.2014.06.011

Pour, A.B., Hashim, M., 2015b. Integrating PALSAR and ASTER data for mineral deposits exploration in tropical environments: a case study from Central Belt, Peninsular Malaysia.

International Journal of Image and Data Fusion, 6(2), 170-188. https://doi.org/10.1080/19479832.2014.985619

Pour, A.B., Hashim, M., 2015c. Hydrothermal alteration mapping from Landsat-8 data, Sar Cheshmeh copper mining district, south-eastern Islamic Republic of Iran. J. Taibah Univ. Sci. 9, 155–166

Pour, A.B., Hashim, M., 2016. Gold mineral prospecting using phased array type l-band synthetic aperture radar (palsar) satellite remote sensing data, central gold belt, Malaysia. The International Archives of the Photogrammetry, Remote Sensing and Spatial Information Sciences, Volume XLI-B8, 2016 XXIII ISPRS Congress, 12–19 July 2016, Prague, Czech Republic. doi:10.5194/isprsarchives-XLI-B8-409-2016

Pour, A.B., Hashim, M., Hong, J.K., Park, Y., 2019a. Lithological and alteration mineral mapping in poorly exposed lithologies using Landsat-8 and ASTER satellite data: north-eastern Graham Land, Antarctic Peninsula. Ore Geol. Rev. 108, 112–133

Pour, A.B., Park, T.S., Park, Y., Hong, J.K., Zoheir, B., Pradhan, B., Ayoobi, I., Hashim, M., 2018b. Application of Multi-Sensor Satellite Data for Exploration of Zn-Pb Sulfide Mineralization in the Franklinian Basin, North Greenland. Remote Sensing, 10, 1186. https://doi.org/10.3390/rs10081186

Pour, A.B., Park, T.-Y.S., Park, Y., Hong, J.K., Muslim, A.M., Läufer, A., Crispini, L., Pradhan, B., Zoheir, B., Rahmani, O., Hashim, M., Hossain, M.S., 2019d. Landsat-8, advanced spaceborne thermal emission and reflection radiometer, and WorldView-3 multispectral satellite imagery for prospecting copper-gold mineralization in the northeastern Inglefield Mobile Belt (IMB), northwest Greenland. Remote Sensing 11 (20), 2430. https://doi.org/10.3390/rs11202430

Pour, A.B., Park, Y., Crispini, L., Läufer, A., Kuk Hong, J., Park, T.-Y.S., Zoheir, B., Pradhan, B., Muslim, A.M., Hossain, M.S., Rahmani, O., 2019c. Mapping Listvenite Occurrences in the Damage Zones of Northern Victoria Land, Antarctica Using ASTER Satellite Remote Sensing Data. Remote Sensing 11, 1408. https://doi.org/10.3390/rs11121408

Pour, A.B., Park, Y., Park, T.S., Hong, J.K., Hashim, M., Woo, J., Ayoobi, I., 2018a. Regional geology mapping using satellite-based remote sensing approach in Northern Victoria Land, Antarctica. Polar Science, 16, 23-46. https://doi.org/10.1016/j.polar.2018.02.004

Pour, A.B., Park, Y., Park, T.S., Hong, J.K., Hashim, M., Woo, J., Ayoobi, I., 2019b. Evaluation of ICA and CEM algorithms with Landsat-8/ASTER data for geological mapping in inaccessible regions. Geocarto International 34(7),785-816. https://doi.org/10.1080/10106049.2018.1434684

Pour, A.B., Sekandari, M., Rahmani, O., Crispini, L., Läufer, A., Park, Y., Hong, J.K., Pradhan, B., Hashim, M., Hossain, M.S., Muslim, A.M., Mehranzamir, K., 2021b. Identification of Phyllosilicates in the Antarctic Environment Using ASTER Satellite Data: Case Study from the Mesa Range, Campbell and Priestley Glaciers, Northern Victoria Land. Remote Sens. 2021, 13, 38. https://doi.org/10.3390/rs13010038

Pour, A.B., Zoheir, B., Pradhan, B., Hashim, M., 2021a. Editorial for the Special Issue: Multispectral and Hyperspectral Remote Sensing Data for Mineral Exploration and Environmental Monitoring of Mined Areas. Remote Sensing 13, 519. https://doi.org/10.3390/rs13030519

Ramli, M. F., Tripathi, N. K., Yusof, N., Shafri, H. Z. M., Ali Rahman, Z., 2009. Lineament mapping in a tropical environment using Landsat imagery. International Journal of Remote Sensing, 30:23, 6277-6300, DOI: 10.1080/01431160902842383

Rezaei, A., Hassani, H., Moarefvand, P., Golmohammadi, A., 2020. Lithological mapping in Sangan region in Northeast Iran using ASTER satellite data and image processing methods. Geology, Ecology, and Landscapes, 4:1, 59-70, DOI:10.1080/24749508.2019.1585657

Richards, J. A., Jia, X., 2006. Remote Sensing Digital Image Analysis An Introduction. 4th ed, Springer-Verlag Berlin Heidelberg, 439P

Sabins, F.F., 1999. Remote sensing for mineral exploration. Ore Geol. Rev. 14, 157–183.

Skakni, O., Hlila, R., Pour, A.B, Martín, M.M., Maate, A., Maate, S., Muslim, A.M., Hossain, M.S. 2020. Integrating remote sensing, GIS and in-situ data for structural mapping over a part of the NW Rif belt, Morocco. Geocarto International, Article in press, https://doi.org/10.1080/10106049.2020.1852611

Salui, C. L., 2018. Methodological Validation for Automated Lineament Extraction by LINE Method in PCI Geomatica and MATLAB based Hough Transformation. Journal Geological Society of India Vol.92, pp.321-328

Sedrette, S., Rebaï, N., 2016. Automatic extraction of lineaments from Landsat Etm+ images and their structural interpretation: Case Study in Nefza region (North West of Tunisia). Journal of Research in Environmental and Earth Sciences, 04, 139-145

Sekandari, M., Masoumi, I., Pour, A.B., Muslim, M. A., Hossain, M.S, Misra, A., 2020b. ASTER and WorldView-3 satellite data for mapping lithology and alteration minerals associated with Pb-Zn mineralization. Geocarto International, Article in press, https://doi.org/10.1080/10106049.2020.1790676

Sekandari, M., Masoumi, I., Pour, A.B., Muslim, M.A., Rahmani, O., Hashim, M., Zoheir, B., Pradhan, B., Misra, A., Aminpour, S.M., 2020a. Application of Landsat-8, Sentinel-2, ASTER and WorldView-3 Spectral Imagery for Exploration of Carbonate-Hosted Pb-Zn Deposits in the Central Iranian Terrane (CIT). Remote Sensing 12, 1239. https://doi.org/10.3390/rs12081239

Sheikhrahimi, A., Pour, A. B., Pradhan, B., Zoheir, B., 2019. Mapping hydrothermal alteration zones and lineaments associated with orogenic gold mineralization using ASTER data: A case study from the Sanandaj-Sirjan Zone, Iran. Advances in Space Research 63, 3315–3332. https://doi.org/10.1016/j.asr.2019.01.035

Shirmard, H., Farahbakhsh, E., Pour, A.B., Muslim, A.M., Müller, R.D., Chandra, R., 2020. Integration of Selective Dimensionality Reduction Techniques for Mineral Exploration Using ASTER Satellite Data. Remote Sensing 12, 1261. https://doi.org/10.3390/rs12081261

Soba, D., 1989. La série de Lom: Etude Géologique et Géochronologique d'un bassin volcanosédimentaire de la Chaîne Panafricaine à l'Est du Cameroun. Thèse Doctorat D'Etat, Université de Paris VI, 198p.

Sonbul, A.R., El-Shafei, M.K., Bishta, A.Z., 2016. Using Remote Sensing Techniques and Field-Based Structural Analysis to Explore New Gold and Associated Mineral Sites Around Al-Hajar Mine, Asir Terrane, Arabian Shield. Journal of African Earth Sciences 117, 285-302. doi: 10.1016/j.jafrearsci.2016.02.009.

Suh, C.E., Lehmann, B., 2003. Morphology and electron-probe microanalysis of residual gold-grain at Dimako, south east Cameroon. Neues Jabrb. für Mineral. Monatsh. 6, 225e275.

Suh, C.E., Lehmann, B., Mafany, G.T., 2006. Geology and geochemical aspects of lode gold mineralization at Dimako- Mboscorro SE Cameroon. Geochem. Explor. Environ. Anal. 6, 295e309.

Sultan, M., Arvidson, R.E., Sturchio, N.C., 1986. Mapping of serpentinites in the Eastern Desert of Egypt using Landsat Thematic Mapper data. Geology 14, 995–999

Suzen. L., Toprak, V., 1998. Filtering of satellite images in geological lineament analyses: An application to a fault zone in Central Turkey, International Journal of Remote Sensing, 19:6, 1101-1114, DOI:10.1080/014311698215621

Takodjou Wambo, J.D., Ganno, S., Afahnwie, N.A., Nomo, N.E., Mvondo, O.J., Nzenti, J.P., 2016. Use of Landsat 7 ETM+ data for the geological structure interpretation: case study of the Ngoura Colomines area, Eastern Cameroon. Journal of Geoscience and Geomatics 4 (3), 61–72.

Takodjou Wambo, J.D., Ganno, S., Djonthu Lahe, Y.S., Kouankap Nono, G.D., Fossi, D.H., Tchouatcha, M.S., Nzenti, J.P., 2018. Geostatistical and GIS analysis of the spatial variability of alluvial gold content in Ngoura-Colomines area, Eastern Cameroon: Implications for the exploration of primary gold deposit. J. Afr. Earth Sc. 142, 138–157.

Takodjou Wambo, J.D., Pour, A.B., Ganno, S., Asimow, P.D., Zoheir, B., Salles, R.d.R., Nzenti, J.P., Pradhan, B., Muslim, A.M., 2020. Identifying high potential zones of gold mineralization in a sub-tropical region using Landsat-8 and ASTER remote sensing data: A case study of the Ngoura-Colomines goldfield, eastern Cameroon. Ore Geol. Rev., 122. doi:10.1016/j.oregeorev.2020.103530.

Tanko Njiosseu, E. L., Nzenti, J.P., Njanko, T., Kapajika, B., Nedelec, A., 2005. New UPb Zircon ages from Tonga (Cameroon): Coexisting Eburnean Transamazonian (2.1 Ga) and Pan-African (0, 6 Ga) imprints. Compte Rendu Géosciences 337, 551-562.

Tata, E., Suh, C.E., Vishiti, A., Shemang, E.M., Fon, N.A., Ateh, K.I., Chombo, N.N., 2018. Wallrock alteration categories and their geochemical signatures in gold-bearing Neoproterozoic granitoids, Batouri gold district, southeastern Cameroon. Geochemistry: Exploration, Environment, Analysis. DOI: 10.1144/geea 2016-017.

Toteu, S.F., Van Schmus, R.W., Penaye, J., Michard, A., 2001. New U-Pb and Sm–Nd data from North-Central Cameroon and its bearing on the Pre–Pan–African history of Central Africa. Precambr. Res. 108, 45–73.

Traore, M., Takodjou Wambo, J.D., Ndepete, C.P., Tekin, S., Pour, A.B., Muslim, A.M., 2020. Lithological and alteration mineral mapping for alluvial gold exploration in the south east of Birao area, Central African Republic using Landsat-8 Operational Land Imager (OLI) data. Journal of African Earth Sciences 170, 103933. https://doi.org/10.1016/j.jafrearsci.2020.103933

Trippa, G.I., Vearncombe, J. R., 2002. Fault/fracture density and mineralization: a contouring method for targeting in gold exploration. Journal of Structural Geology 26 (2004), 1087–1108

Vishiti, A., Suh, C.E., Etame, J., 2019. Features of gold-bearing quartz veins in an artisanal mining dominated terrain, Batouri gold district, Eastern region of Cameroon. IUGS, Episodes Vol. 42, No. 3, 199-212.

Vishiti, A., Suh, C.E., Lehmann, B., Shemang, E.M., Ngome, N.L.J., Nshanji, N.J., Chinjo,E.F., Mongwe, O.Y., Egbe, A.J., Petersen, S., 2017. Mineral chemistry, bulk rock geochemistry, and S-isotope signature of lode-gold mineralization in the Bétaré Oya gold district, south-east Cameroon. Geological journal 2017, 1-18.

Yousefi, T., Aliyari, F., Abedini, A., C alagari A. A., 2018. Integrating geologic and Landsat-8 and ASTER remote sensing data for gold exploration: a case study from Zarshuran Carlin-type gold deposit, NW Iran. Arabian Journal of Geosciences 11, 482. https://doi.org/10.1007/s12517-018-3822-x

Yu, L., Porwal, A., Holden, E-J., Dentith, M.C., 2012. Towards automatic lithological classification from remote sensing data using support vector machines. Computers & Geosciences 45, 229–239. doi:10.1016/j.cageo.2011.11.019

Zhang, X., Pazner, M., Duke, N., 2007. Lithologic and mineral information extraction for gold exploration using ASTER data in the south chocolate mountains (California). ISPRS Journal of Photogrammetry & Remote Sensing, 62, 271–282. doi:10.1080/01431160903124682

Zoheir, B., El-Wahed, M.A., Pour, A.B., Abdelnasser, A., 2019a. Orogenic gold in transpression and transtension zones: Field and remote sensing studies of the Barramiya-Mueilha sector, Egypt. Remote Sensing 11 (18), 2122. https://doi.org/10.3390/rs11182122

Zoheir, B., Emam, A., 2013. Field and ASTER imagery data for the setting of gold mineralization in Western Allaqi–Heiani belt, Egypt: A case study from the Haimur deposit. Journal of African Earth Sciences 99 (1) 150–164

Zoheir, B., Emam, A., Abdel-Wahed, M., Soliman, N., 2019b. Multispectral and Radar Data for the Setting of Gold Mineralization in the South Eastern Desert, Egypt. Remote Sensing 11, 1450. https://doi.org/10.3390/rs11121450

Figure captions

Figure 1: Geology of southeastern Cameroon. (a) Geological map of Cameroon (modified after Toteu et al., 2001). Showing (1) northern domain; (2) a center domain and (3) a southern domain. The Central African Shear Zone is defined by a system of NE-trending faults including the Tchollire-Banyo Fault (TBF), the Adamawa Fault (AF), the Sanaga Fault (SF), and the Kribi-Campo Fault (KCF). The inset map of the African continent shows the location of Cameroon relative to the distribution of cratons and mobile belts. (b) Regional geological map of southeastern Cameroon showing artisanal gold mining sites and other reported gold indications (modified after Milési et al., 2004).

Figure 2: Flowchart methodology

Figure 3: PCs images highlighting hydrothermal alterations. A: PC8-2 highlighting ferrous minerals; B: PC8-5 highlighting iron oxydes/hydroxydes; C: PC8-4 highlighting clay and carbonate minerals; D: PC image composite highlighting clay and carbonate minerals, ferrous minerals and iron oxydes/hydroxydes in RGB.

Figure 4: Band ratio images highlighting hydrothermal alterations: (A) Band ratio 6/7 for clay and carbonate minerals; (B) Band ratio 6/5 highlighting ferrous minerals; (C) Band ratio 4/2 showing iron oxydes/hydroxydes; (D) FCC highlighting iron oxydes/hydroxydes, ferrous minerals and clay and carbonate minerals in RGB.

Figure 5: Lineaments extracted from OLI (A) and ETM+ (B) images.

Figure 6: Number of lineaments extracted from different enhancement/edge detection methods for OLI and ETM+ images.

Figure 7: Statistical analysis of lineament networks. Histogram of lineament length distributions as a function of their number of OLI (A) and ETM+ (B) data. (C) Distribution frequency of lineament lengths as a function of their number from OLI + ETM+ data.

Figure 8: Directional rosette of lineaments obtained from the data: (A) OLI + ETM+, (B) OLI, (C) ETM+.

Figure 9: MNF image and vegetation. (A): MNF_{123} FCC; (B): NDVI

Figure 10: Field evidence: (A) migmatitic dome; (B) granite slab; (C) pink granite ball outcrop; (D) porphyritic granite slab; (E) amphibolite enclave ; (F) mylonite dome.

Figure 11: Geologic map of the study area (modified from Gazel and Gerard, 1954).

Figure 12: Gold mineralization occurrences: (A) Open pit for artisanal gold mining. (B) Smoky and brecciated gold quartz veins mined for gold production at Kana. (C) Outcrop of sulphide porphyritic rock and (D) quartz vein showing a hydrothermal alteration zone.

Figure 13: Structural field data: (A) Metamorphic foliation S1 in a Melanocratic gneiss enclave, (B) Sm mylonitic schistosity in an orthogneiss package showing dextral rotation, (C) C_2 strike slip showing dextral polarity, (D) P_2 fold showing dextral polarity, (E) P_3 fold with stuffed hinge, (F) fracture directional rosette.

Figure 14: Litho-structural map of the study area

Figure 15: Lineament directional rosette around the seven main mining sites (A) and a Lineaments density map (B)

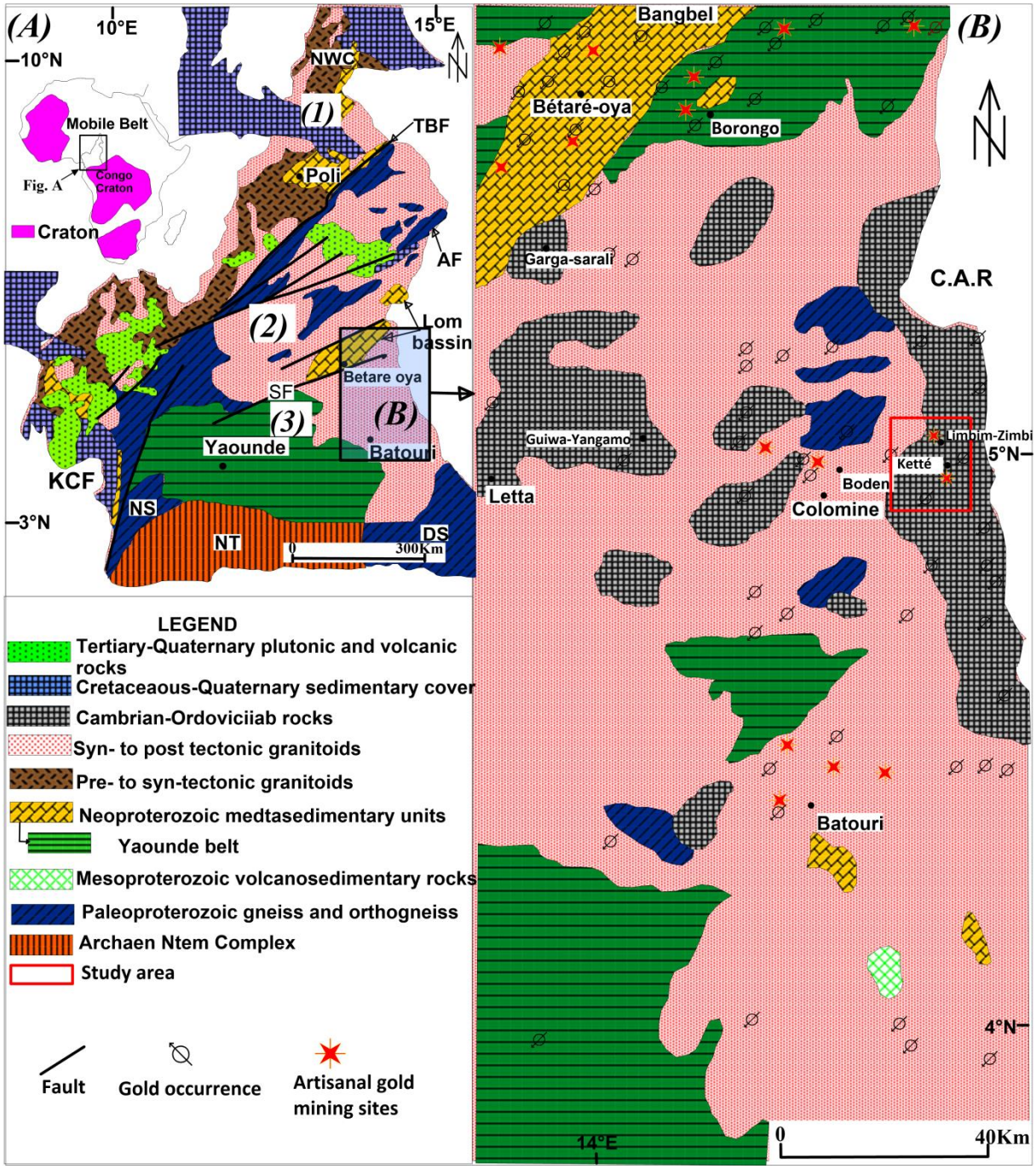
(A)
10°E
15°E
10°N
3°N
NWC
(1)
TBF
Mobile Belt
Congo Craton
Fig. A
Craton
Poli
AF
(2)
Lom bassin
Betare oya
SF
(3)
(B)
Yaounde
Batouri
KCF
NS
NT
DS
0
300Km
LEGEND
Tertiary-Quaternary plutonic and volcanic rocks
Cretaceaous-Quaternary sedimentary cover
Cambrian-Ordoviciiab rocks
Syn- to post tectonic granitoids
Pre- to syn-tectonic granitoids
Neoproterozoic medtasedimentary units
Yaounde belt
Mesoproterozoic volcanosedimentary rocks
Paleoproterozoic gneiss and orthogneiss
Archaen Ntem Complex
Study area
Fault
Gold occurrence
Artisanal gold mining sites
Bangbel
(B)
Bétaré-oya
Borongo
Garga-sarali
C.A.R
Guiwa-Yangamo
Limbim-Zimbi
Ketté
5°N
Boden
Letta
Colomine
Batouri
4°N
14°E
0
40Km

Figure 1

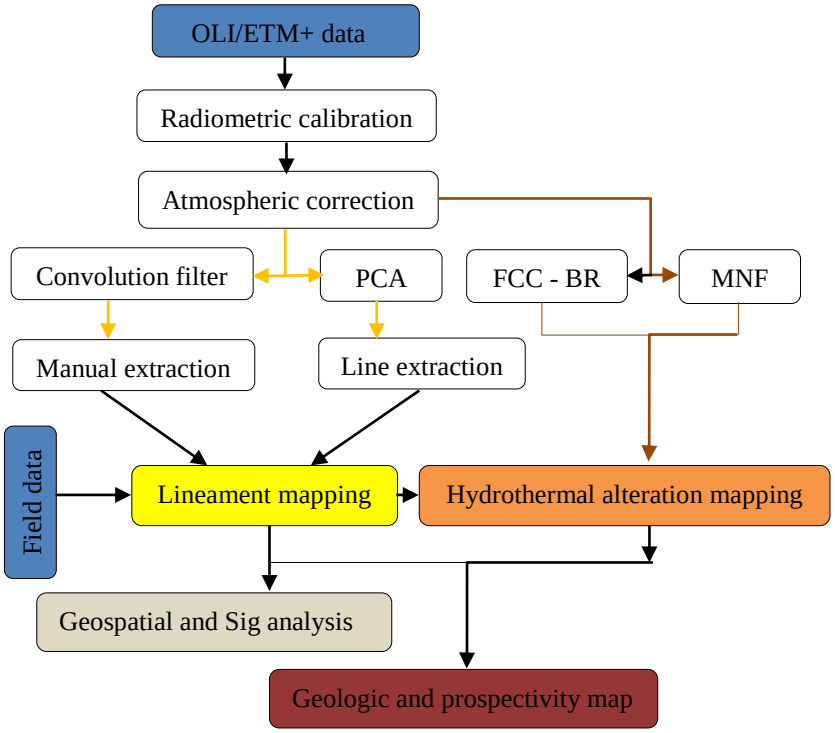
OLI/ETM+ data
Radiometric calibration
Atmospheric correction
Convolution filter
PCA
FCC - BR
MNF
Manual extraction
Line extraction
Field data
Lineament mapping
Hydrothermal alteration mapping
Geospatial and Sig analysis
Geologic and prospectivity map

Figure 2

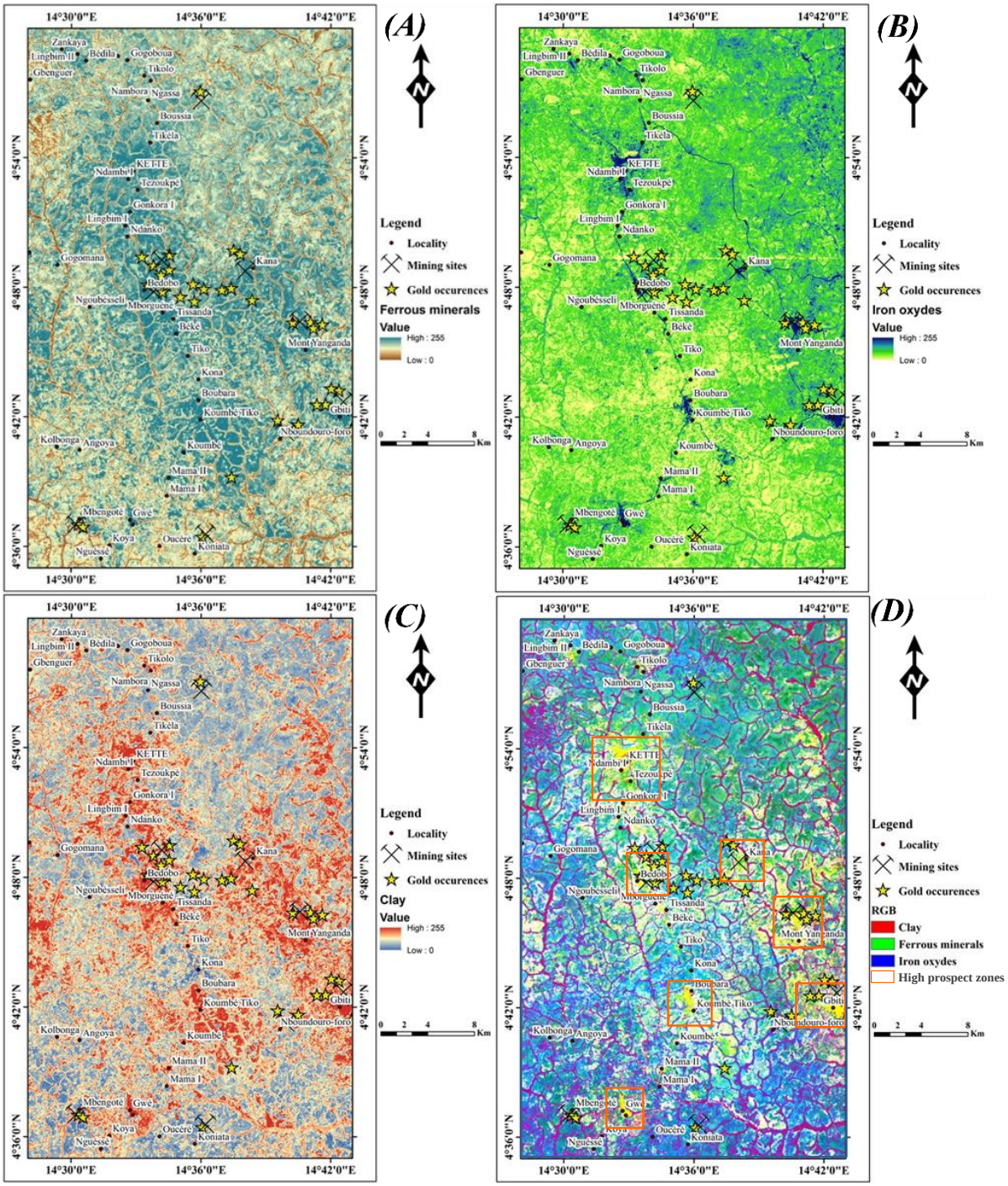
(A)
(B)
(C)
(D)
14°30'0"E
14°36'0"E
14°42'0"E
4°54'0"N
4°48'0"N
4°42'0"N
4°36'0"N
Zankaya
Lingbim II
Bédila
Gogoboua
Tikolo
Gbenguer
Nambora
Ngassa
Boussia
Tikéla
KETTE
Ndambi I
Tezoukpé
Gonkora I
Lingbim I
Ndanko
Gogomana
Kana
Bédobo
Ngoubésseli
Mborguené
Tissanda
Béké
Mont Yanganda
Tiko
Kona
Boubara
Koumbé Tiko
Gbiti
Nboundouro-foro
Kolbonga
Angoya
Koumbé
Mama II
Mama I
Mbengoté
Gwé
Koya
Oucéré
Nguéssé
Koniata
Legend
Locality
Mining sites
Gold occurences
Ferrous minerals
Iron oxydes
Clay
RGB
Clay
Ferrous minerals
Iron oxydes
High prospect zones
Value
High : 255
Low : 0
0 2 4 8 Km

Figure 3

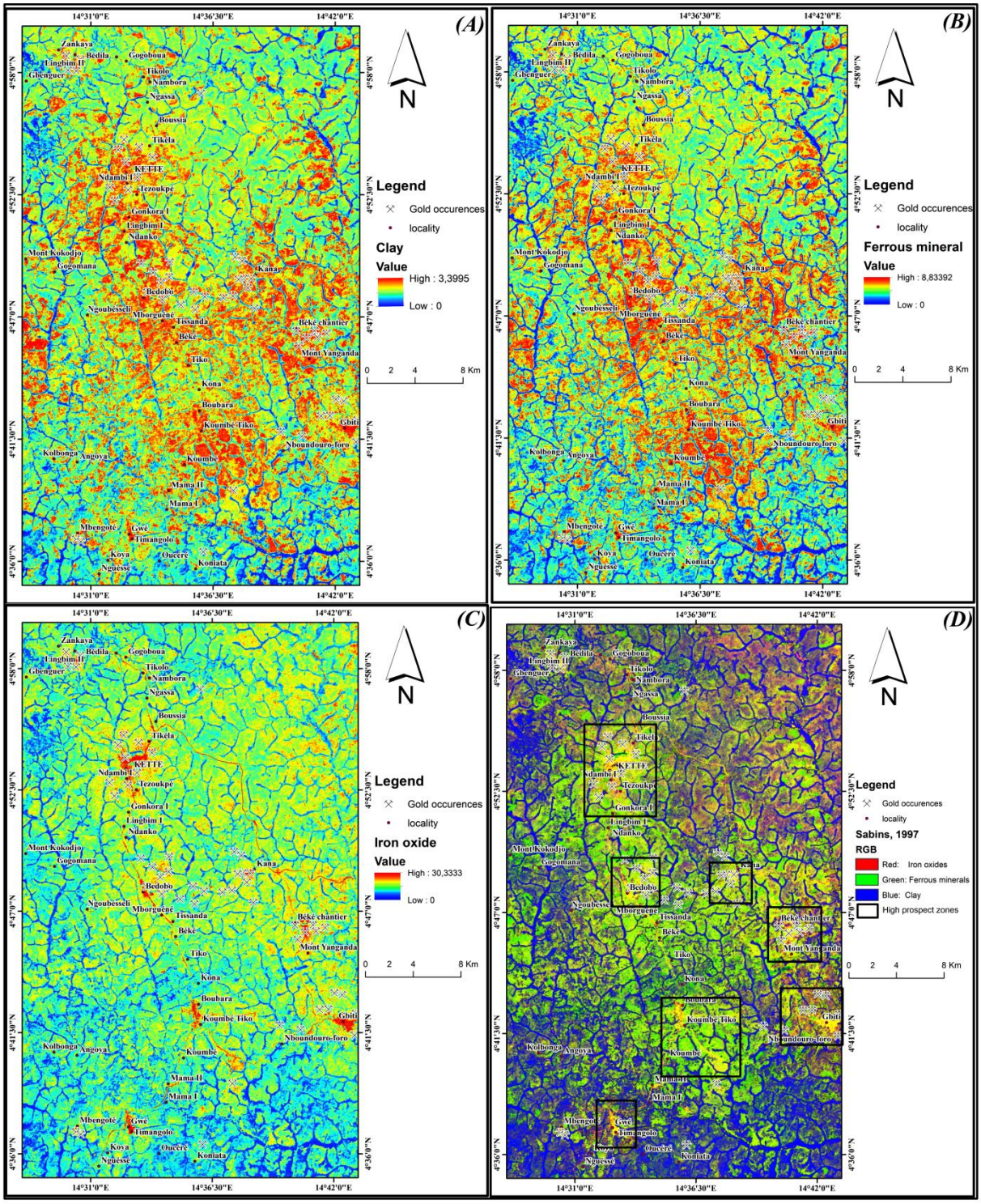
(A)
(B)
(C)
(D)
14°31'0"E
14°36'30"E
14°42'0"E
4°58'0"N
4°52'30"N
4°47'0"N
4°41'30"N
4°36'0"N
N
Legend
Gold occurences
locality
Clay
Value
High : 3,3995
Low : 0
Ferrous mineral
Value
High : 8,83392
Low : 0
Iron oxide
Value
High : 30,3333
Low : 0
Sabins, 1997
RGB
Red: Iron oxides
Green: Ferrous minerals
Blue: Clay
High prospect zones
0 2 4 8 Km
Zankaya
Bedila
Gogoboua
Lingbim II
Gbenguer
Tikolo
Nambora
Ngassa
Boussia
Tikela
KETTE
Ndambi I
Tezoukpe
Gonkora I
Lingbim I
Ndanko
Mont Kokodjo
Gogomana
Kana
Bedobo
Ngoubesseli
Mborguene
Tissanda
Béke
Béke chantier
Mont Yanganda
Tiko
Kona
Boubara
Koumbe Tiko
Gbiti
Nboundouro foro
Koumbe
Kolbonga
Angoya
Mama II
Mama I
Mbengolé
Gwé
Timangolo
Koya
Nguessé
Oucéré
Koniata

Figure 4

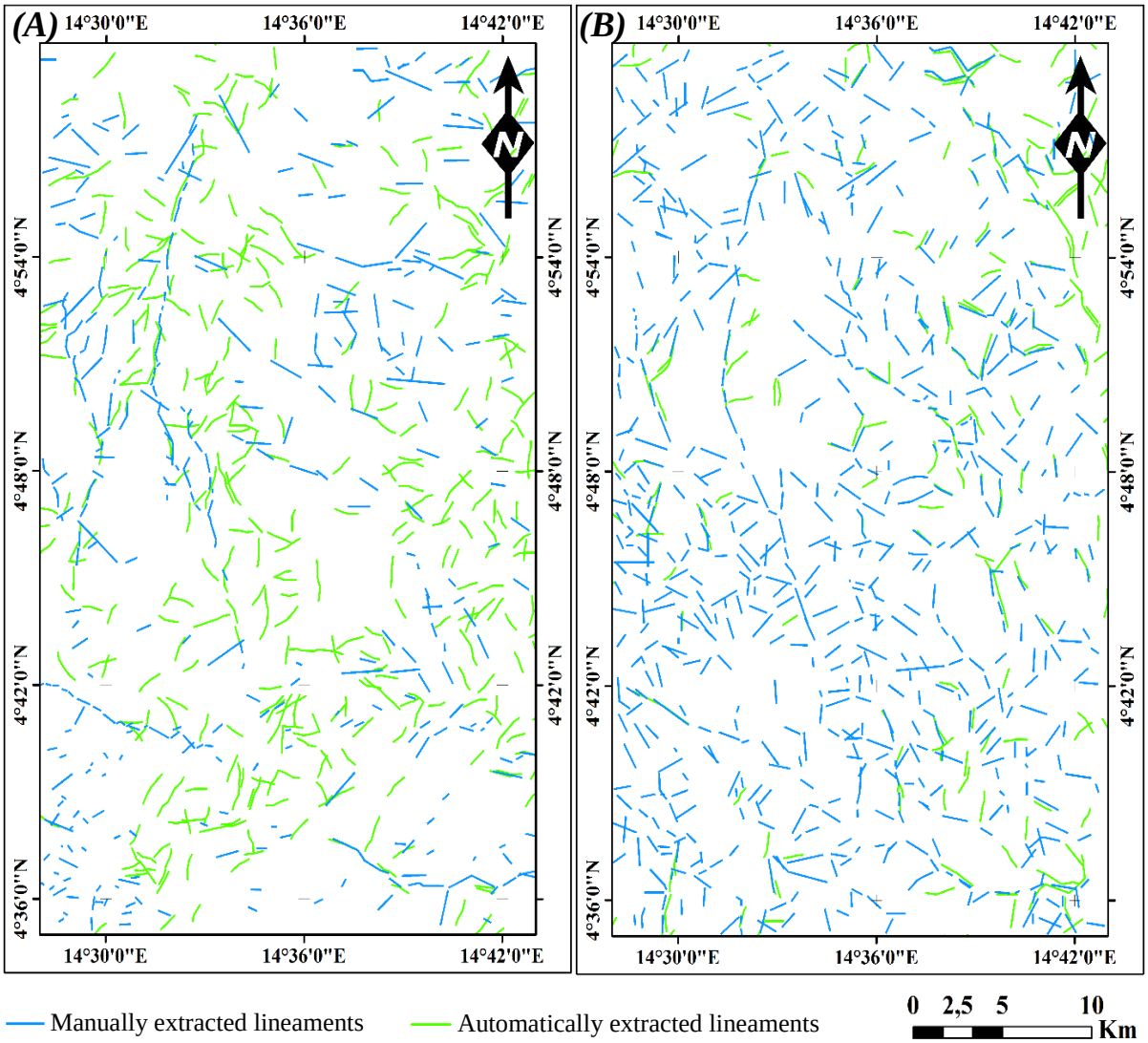

Figure 5

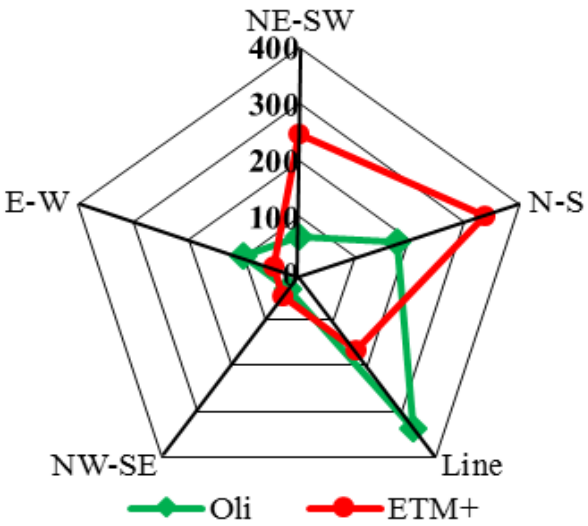

Figure 6

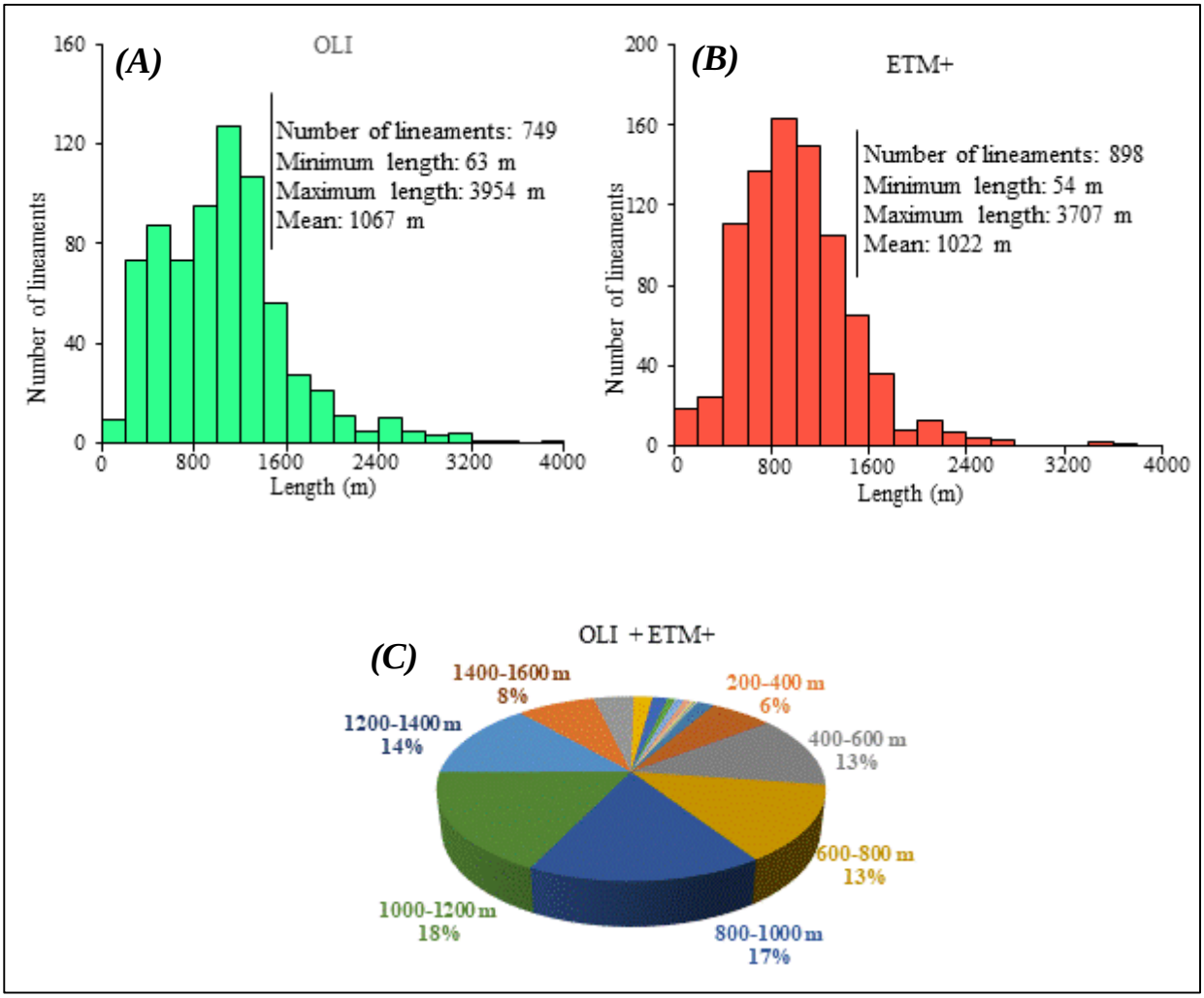

Figure 7

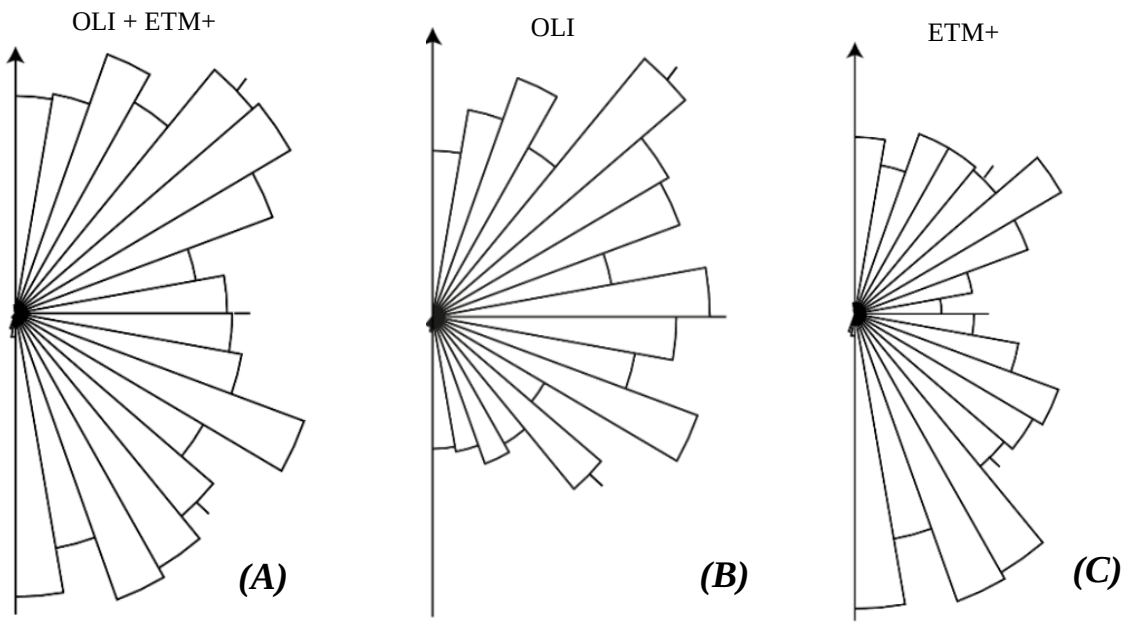

Figure 8

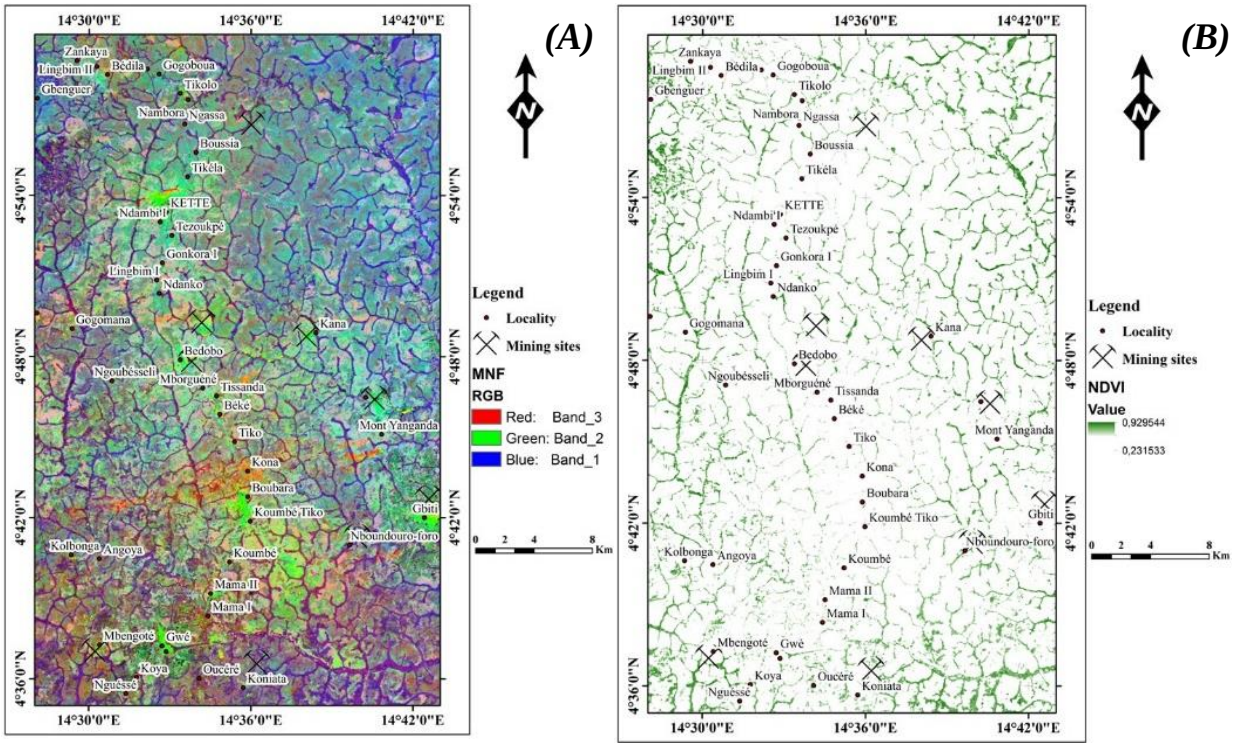
(A)
(B)
14°30'0"E
14°36'0"E
14°42'0"E
4°54'0"N
4°48'0"N
4°42'0"N
4°36'0"N
Zankaya
Lingbim II
Bédila
Gogoboua
Gbenguer
Tikolo
Nambora
Ngassa
Boussia
Tikéla
KETTE
Ndambi II
Tezoukpé
Gonkora I
Lingbim I
Ndanko
Gogomana
Kana
Bedobo
Ngoubésseli
Mborguéné
Tissanda
Béké
Mont Yanganda
Tiko
Kona
Boubara
Koumbé Tiko
Gbiti
Kolbonga
Angoya
Koumbé
Nboundouro-foro
Mama II
Mama I
Mbengoté
Gwé
Koya
Oucéré
Koniata
Nguéssé
Legend
Locality
Mining sites
MNF
RGB
Red: Band_3
Green: Band_2
Blue: Band_1
NDVI
Value
0,929544
0,231533
0 2 4 8 Km

Figure 9

Figure 10

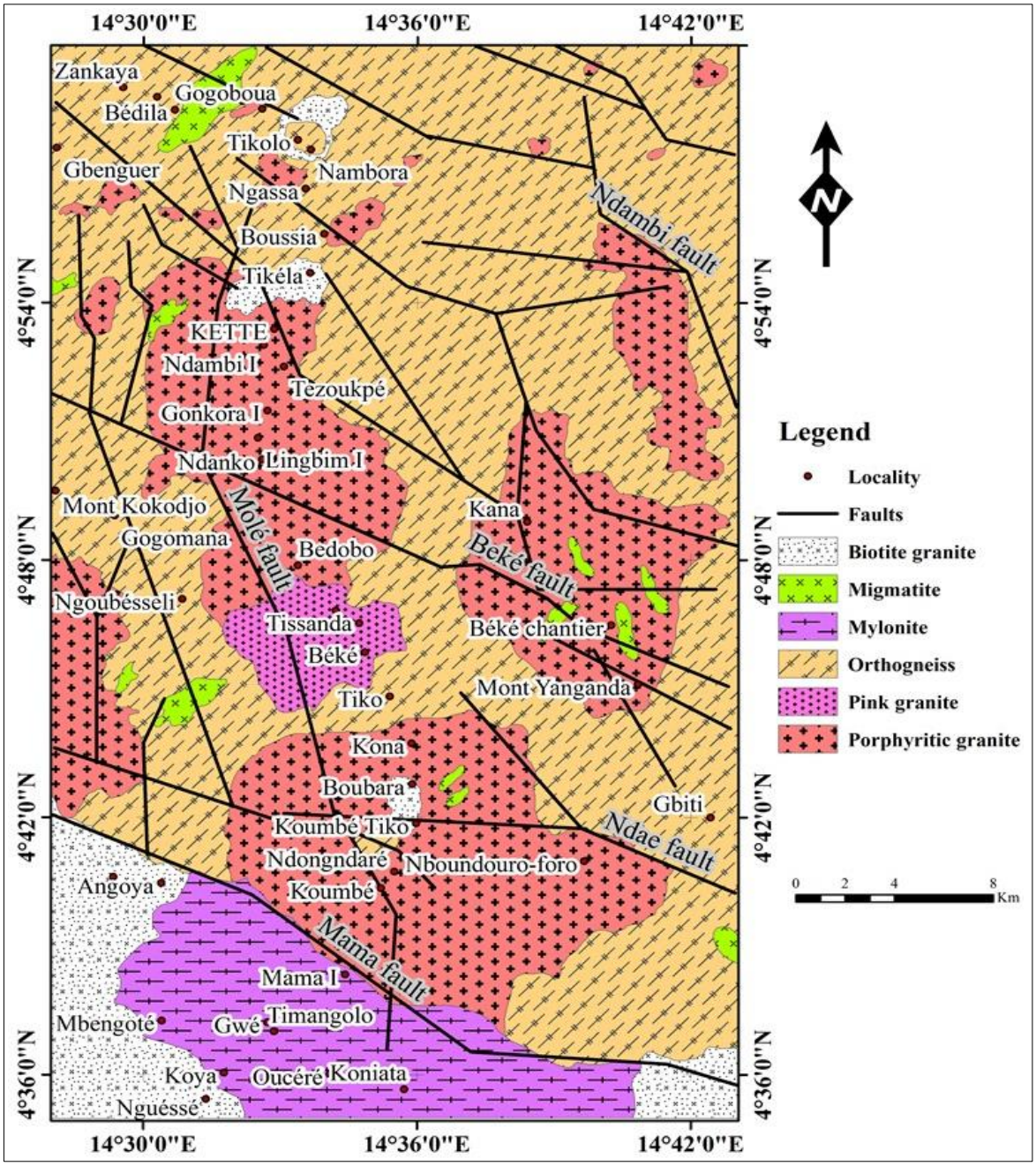
14°30'0"E
14°36'0"E
14°42'0"E
4°54'0"N
4°48'0"N
4°42'0"N
4°36'0"N
Zankaya
Gogoboua
Bédila
Tikolo
Nambora
Gbenguer
Ngassa
Boussia
Tikéla
KETTE
Ndambi I
Tezoukpé
Gonkora I
Ndanko
Lingbim I
Mont Kokodjo
Gogomana
Molé fault
Bedobo
Ngoubésseli
Tissanda
Béké
Tiko
Kana
Béké fault
Béké chantier
Mont Yanganda
Kona
Boubara
Koumbé Tiko
Ndongndaré
Nboundouro-foro
Koumbé
Gbiti
Ndae fault
Angoya
Mama fault
Mama I
Timangolo
Mbengoté
Gwé
Koya
Oucéré
Koniata
Nguéssé
Ndambi fault
N
Legend
Locality
Faults
Biotite granite
Migmatite
Mylonite
Orthogneiss
Pink granite
Porphyritic granite
0 2 4 8
Km

Figure 11

Figure 12

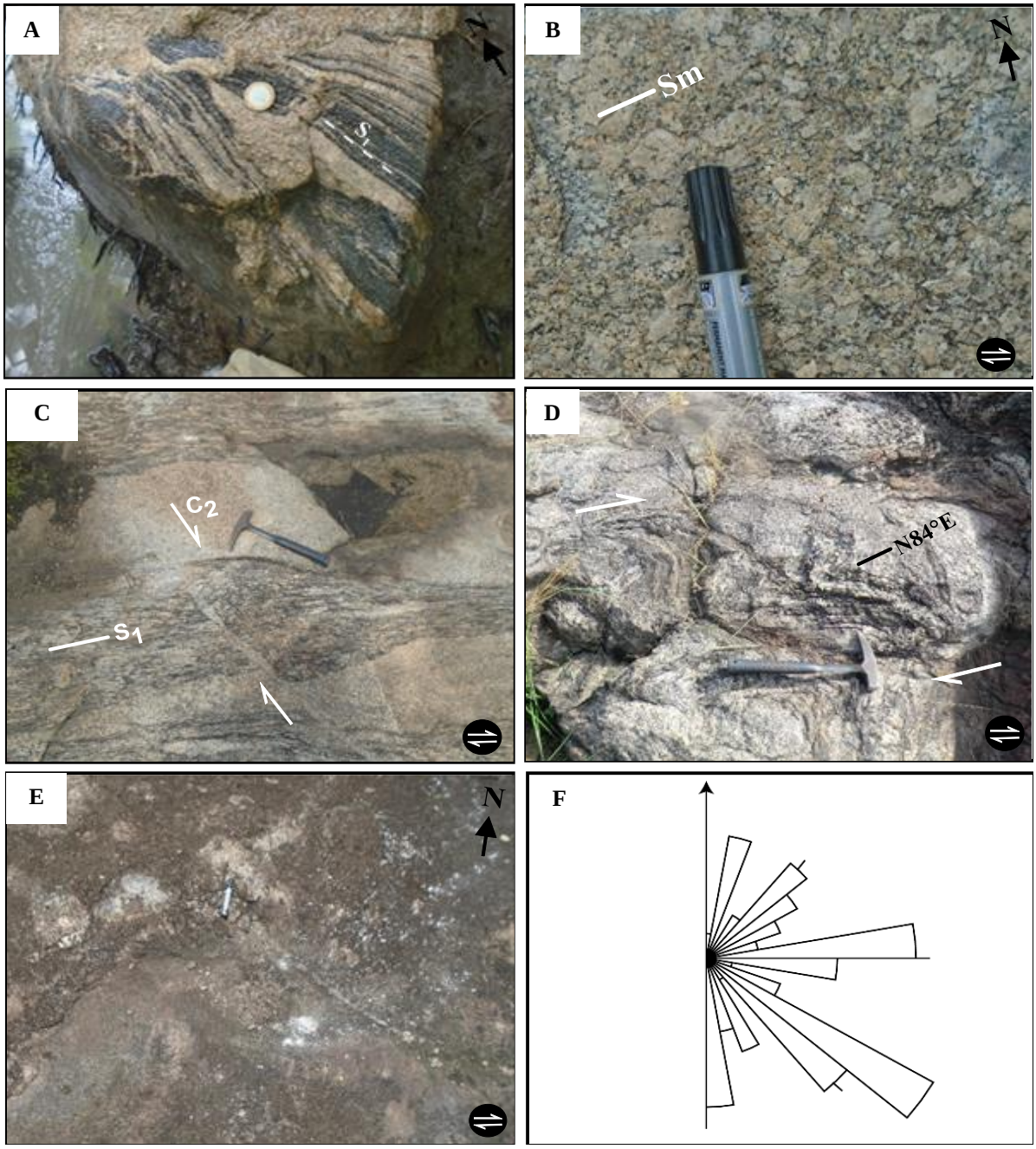

Figure 13

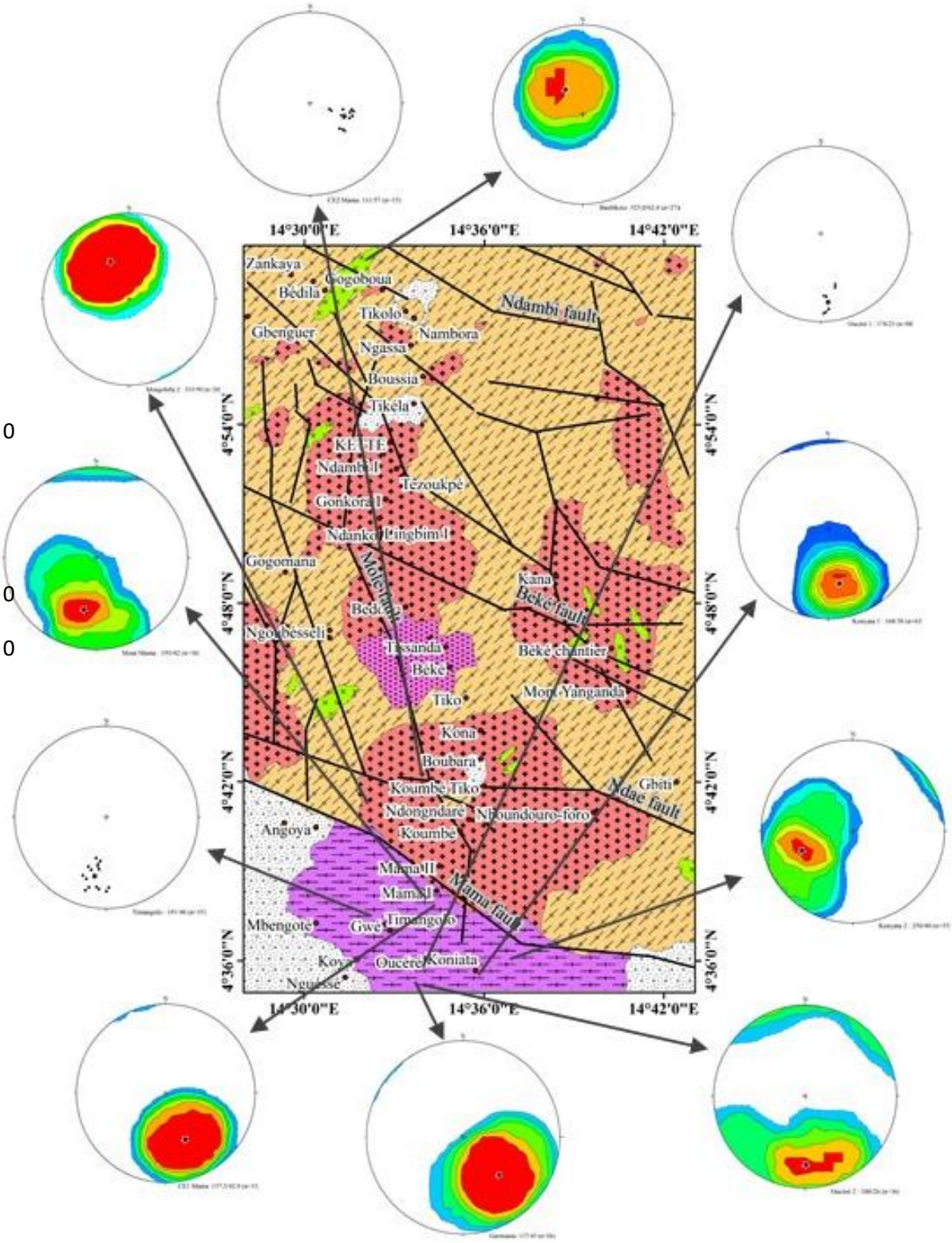
14°30'0"E
14°36'0"E
14°42'0"E
4°54'0"N
4°48'0"N
4°42'0"N
4°36'0"N
Zankaya
Bédila
Gogoboua
Tikolo
Nambora
Gbenguer
Ngassa
Boussia
Tikéla
Ndambi fault
Tézoukpé
Gonkora I
Gogomana
Kana
Béké fault
Béké chantier
Mont Yangandà
Tissanda
Béké
Tiko
Kona
Boubara
Koumbe Tiko
Ndongndaré
Ngoundouré-foro
Koumbé
Gbiti
Ndae fault
Angoya
Mama II
Mama I
Mama fault
Mbengoté
Gwé
Koya
Oucéré
Koniata
Nguasse

Figure 14

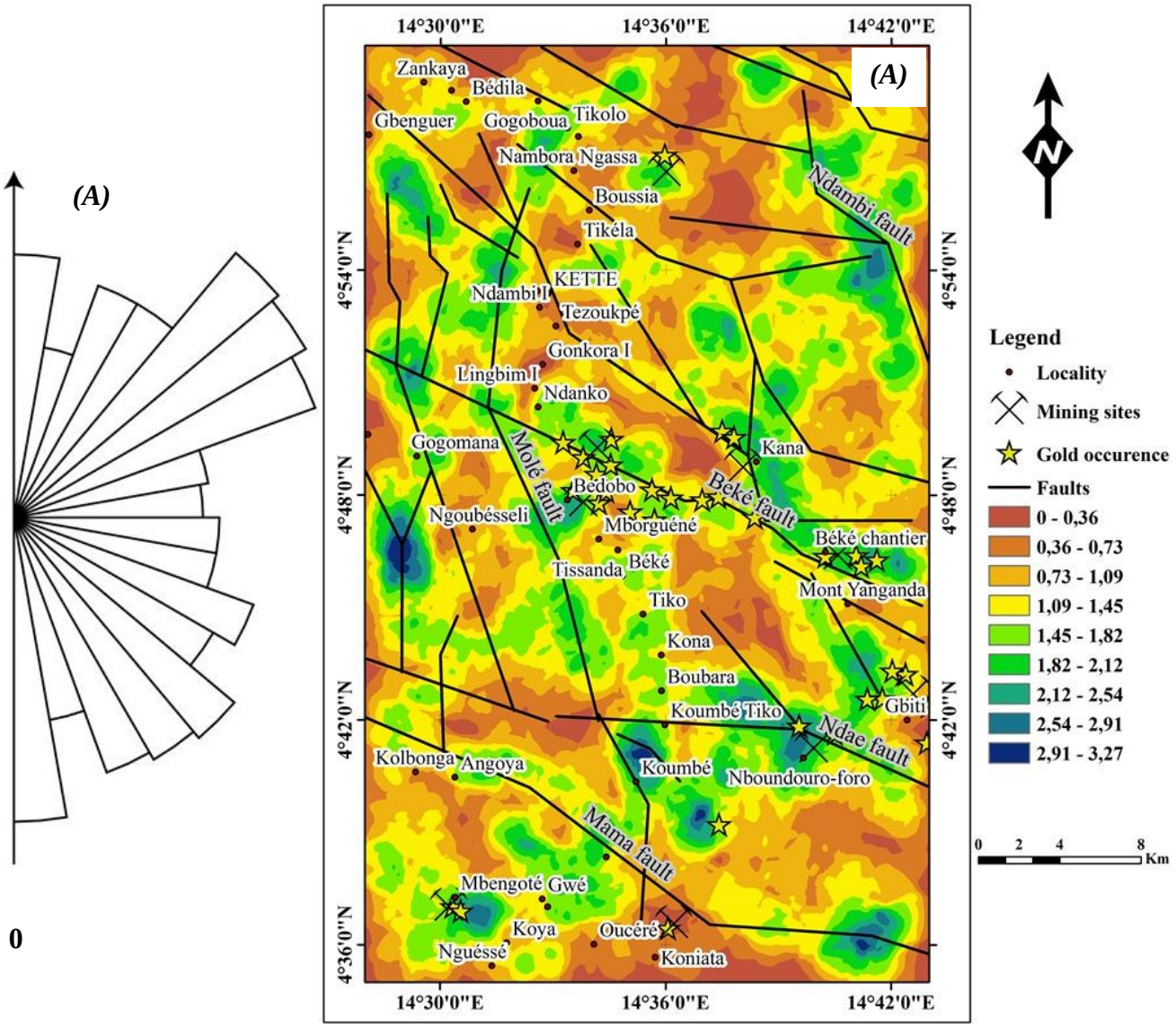
(A)
0
14°30'0"E
14°36'0"E
14°42'0"E
4°54'0"N
4°48'0"N
4°42'0"N
4°36'0"N
Zankaya
Bédila
Gbenguer
Gogoboua
Tikolo
Nambora
Ngassa
Boussia
Tikéla
KETTE
Ndambi I
Tezoukpé
Gonkora I
Lingbim I
Ndanko
Gogomana
Kana
Bédobo
Ngoubésseli
Mborguéné
Tissanda
Béké
Tiko
Kona
Boubara
Koumbé
Tiko
Kolbonga
Angoya
Koumbé
Nboundouro-foro
Mbengoté
Gwé
Koya
Oucéré
Nguéssé
Koniata
Gbiti
Mont Yanganda
Béké chantier
Ndambi fault
Molé fault
Béké fault
Ndae fault
Mama fault
N
Legend
Locality
Mining sites
Gold occurence
Faults
0 - 0,36
0,36 - 0,73
0,73 - 1,09
1,09 - 1,45
1,45 - 1,82
1,82 - 2,12
2,12 - 2,54
2,54 - 2,91
2,91 - 3,27
0 2 4 8
Km

Figure 15